

UC Berkeley

UC Berkeley Electronic Theses and Dissertations

Title

A Study on Seismic Behavior of Reinforced Concrete Arch Ribs

Permalink

<https://escholarship.org/uc/item/08h3d6g0>

Author

De la Mora Bayardo, Diego

Publication Date

2024

Peer reviewed|Thesis/dissertation

A Study on Seismic Behavior of Reinforced Concrete Arch Ribs

By

Diego De la Mora Bayardo

A dissertation submitted in partial satisfaction of the
requirements for the degree of

Doctor of Philosophy

in

Engineering – Civil and Environmental Engineering

in the

Graduate Division

of the

University of California, Berkeley

Committee in charge:

Professor Jack P. Moehle

Professor Matthew DeJong

Professor Jon Wilkening

Summer 2024

A Study on Seismic Behavior of Reinforced Concrete Arch Ribs

Copyright 2024

by

Diego De la Mora Bayardo

Abstract

A Study on Seismic Behavior of Reinforced Concrete Arch Ribs

by

Diego De la Mora Bayardo

Doctor of Philosophy in Engineering - Civil and Environmental Engineering

University of California, Berkeley

Professor Jack P. Moehle, Chair

Reinforced concrete arch bridges face unique challenges due to high axial forces that can compromise their ductile flexure response under seismic conditions. Currently, arch bridges in California do not have any special design requirements despite their unique geometry. This dissertation, through experimental testing and numerical model analysis, evaluates the impact of axial loads on displacement capacity, compares it with the current Caltrans design requirements, and aims to recommend transverse reinforcement configurations and detailing for enhanced seismic performance.

This dissertation is divided into three sections. The first section is an extensive experimental program consisting of nine 1/3 scale reinforced concrete specimens that replicate the critical region of a bridge arch rib. The represented bridges are arch bridges designed and constructed by the California Department of Transportation. The specimens were tested under moderate and high axial loads with increasing reversed cyclic displacement amplitudes. Observations of the physical tests are presented. Experimental results demonstrate that an increase in the volume of transverse reinforcement proportionally increases the deformation capacity; closer transverse reinforcement spacing is crucial for ensuring ductile behavior; and high axial force reduces the displacement ductility capacity of the member and produces severe damage in the core at large drifts. The second section describes how the physical test data was used to calibrate fiber models of an arch rib segment to perform a parametric study to investigate key variables such as section geometry, transverse reinforcement configuration, and axial force ratio. Results show consistency with the experimental data. Expressions to predict the ultimate drift capacity for circular-confined sections and square-confined sections are presented. The third section introduces a methodology to investigate the dynamic behavior of reinforced concrete arch bridges. Results of the proposed methodology include the development of fragility functions and engineering demand parameters hazard curves using hazard-consistent ground motions.

Contents

Chapter 1	1
1.1 Overview	1
1.2 Research Objectives and Scope of work	1
1.3 Report Organization	2
Chapter 2	3
2.1 Abstract	3
2.2 Introduction	3
2.3 Literature Review	4
2.4 Research Significance	5
2.5 Test Specimen Configurations	5
2.6 Materials	8
2.7 Testing	10
2.8 Instrumentation	11
2.9 Test Observations	12
2.10 Overall Measured Results	14
2.11 Discussion	18
2.12 Conclusions	20
2.13 Bibliography	20
Chapter 3	22
3.1 Abstract	22
3.2 Introduction	22
3.3 Research Significance	23
3.4 Literature Review	23
3.5 Finite Element-Model	25
3.6 Calibration and Model Validation	28
3.7 Parametric Studies	37
3.8 Discussion	42
3.9 Conclusions	45
3.10 Bibliography	46
Chapter 4	48
4.1 Introduction	48

4.2	Literature Review	48
4.3	Methodology for Risk Analysis on Arch Bridges	51
4.4	Bibliography	54
Chapter 5	55
5.1	Summary	55
5.2	Conclusions	57
5.3	Design Recommendations.....	59
Appendix A.	61
A.1.	Specimen Photographs.....	61
A.1.1.	Specimen 5	61
A.1.2.	Specimen 6	63
A.1.3.	Specimen 7	65
A.1.4.	Specimen 8	67
A.1.5.	Specimen 9	70
Appendix B.	72
B.1.	Instrumentation	72
B.2.	Reinforcement steel properties	77

List of Figures

Figure 2.1. General specimen dimensions.	6
Figure 2.2. Stress-Strain relationships of the reinforcing steel used in tests.	8
Figure 2.3. Loading frame configuration.	10
Figure 2.4. Forces applied in the specimen during testing.	10
Figure 2.5. Global view of test specimen during testing.	11
Figure 2.6. Specimen deformed shape during testing.	11
Figure 2.7. Instrumentation photograph. Linear potentiometers on south face.	12
Figure 2.8. Post test photographs.	14
Figure 2.9. Specimens Moment-Drift relationship.	17
Figure 2.10. Volumetric confinement Ratio - Drift Ratio Relationship.	19
Figure 3.1. (a) Experimental arch rib Specimen dimensions. (b) Discrete structural model.	26
Figure 3.2. Typical strain-stress relationship for the materials utilized in analytical models.	28
Figure 3.3. Fiber section meshes.	30
Figure 3.4. Moment-drift ratio relationships, and Moment-drift ratio backbones for Sections Type S.	31
Figure 3.5. Moment-drift and moment-curvature comparison for Specimen 4 model with different ultimate confined concrete strain input.	32
Figure 3.6. Moment-drift ratio relationships, and Moment-drift ratio backbones for Sections Type P.	33
Figure 3.7. Moment-drift ratio relationships, and Moment-drift ratio backbones for Sections Type H.	34
Figure 3.8. Moment-drift comparison for Specimen 9 model with different ultimate confined concrete strain input.	35
Figure 3.9. Experimental and Analytical moment-curvature relationships.	36
Figure 3.10. Parametric models Moment-Drift relationship.	41
Figure 3.11. Volumetric confinement Ratio - Drift Ratio Relationship.	43
Figure 4.1. Overview of the PEER PBEE framework.	51
Figure 4.2. SDOF system with effective modal mass and effective modal height for the nth mode.	52
Figure 4.3. Combined Response Spectra for several Hazard Levels conditioned at $T=2s$	53
Figure A.1.1. Specimen 5 photographs.	62
Figure A.1.2. Specimen 6 photographs.	64

Figure A.1.3. Specimen 7 photographs.....	66
Figure A.1.4. Specimen 8 photographs.....	69
Figure A.1.5. Specimen 9 photographs.....	71
Figure B.1. Instrumentation photographs.....	72
Figure B.2. Instrumentation for global deformations.....	73
Figure B.3. Strain gauge locations.....	74
Figure B.4. Linear potentiometer gauge lengths.....	75
Figure B.5. Fiber optic replacement.....	76

List of Tables

Table 2.1. Properties and details of test specimen	9
Table 2.2. Experimental results summary.	18
Table 3.1. Properties and details of test specimens.....	29
Table 3.2. Material input parameters for Beam-Column Element Fiber Sections Type S.....	30
Table 3.3. ReinforcingSteel input parameters for analytical models.	31
Table 3.4. Material input parameters for Beam-Column Element Fiber Section Type P.....	33
Table 3.5. Material input parameters for Beam-Column Element Fiber Sections Type H.	34
Table 3.6. Experimental and analytical calibration results summary.....	36
Table 3.7. Principal parameters in analytical models.	38
Table 3.8. Ultimate confined concrete strain capacity.	39
Table 3.9. Concrete04 input parameters for parametric models.	40
Table 3.10. Parametric models results summary.....	42
Table 3.11. Experimental or analytical ultimate displacement drift versus predicted ultimate displacement drift for sections with circular confinement.....	44
Table 3.12. Experimental or analytical ultimate displacement drift versus predicted ultimate displacement drift for sections with square confinement and double-headed bars cross-ties.....	45
Table 5.1. Summary of properties and details of test specimens.	56
Table B.5.2. Linear potentiometer gauge lengths.	75
Table B.5.3. Reinforcing steel properties.....	77

Acknowledgments

I would like to start by expressing my deepest gratitude to my advisor, Professor Jack Moehle, for his continuous support, exceptional guidance, and insightful feedback throughout my PhD. His mentorship and example have been instrumental in shaping my development as a researcher and critical thinker. I'm truly grateful for working with him on my doctoral research journey.

I am immensely thankful to Daniel Miller, whose previous research laid a strong foundation for this study. His guidance during my initial steps into the experimental project and his mentorship, meetings, and calls were invaluable in allowing me to continue the experimental program successfully. Daniel's willingness to share experimental data, post-processing tools, and ideas without hesitation greatly contributed to the realization of this work.

I am also grateful to the Davis Hall laboratory staff, Shakhzod Takhirov, Matthew Cataleta, Philip Wong, Cruz Carlos, and Llyr Griffith, whose expertise and dedication were instrumental in the success of the experimental program. Additionally, I extend my thanks to the undergraduate students Zane Schemmer, Max Braunstein, Kevin McEntee, Emily Wu, Jenna Cheng, Daniel Ornelas, Mikayla Haas, and Kendall Thach for their hard work in building and instrumenting the test specimens. Their enthusiasm and dedication were a great source of motivation for me. My time at the Davis Hall laboratory was full of friends who shared my passion for knowledge and civil engineering.

I would like to thank the members of my dissertation committee, Prof. Matthew DeJong and Prof. Jon Wilkening, as well as the members of my qualifying exam committee, Prof. Tracy Becker and Prof. Norman Abrahamson. Their invaluable advice, feedback, and encouragement have greatly contributed to the quality and completion of this work.

I am grateful to my research group members over the years, Tali Feinstein, Ben Worsfold, Connie Chen, Jerry Zhai, Han Liu, Camila Lopez, Jorge Archbold, and Daniel Gaspar, for their camaraderie, intellectual exchanges, and friendship. Thanks to Carlos Arteta for his support and bright ideas.

I am also thankful to my housemates over these years, Sebastian Prillo, Juan Manuel Perez-Bertoldi, Irene Farah, Daniela Orellana, Ali El Hajj Chegade, Logan Smesrud, and Silvia Farina, for their friendship and great memories together.

Special thanks to Sofia Herrera for her unconditional support, unforgettable adventures, and never-ending patience since I started studying civil engineering. Her encouragement and love have been a constant source of strength.

Finally, I am deeply grateful to my friends, professors, and family in Mexico for their constant support and motivation throughout these years.

The California Department of Transportation supported the work presented in this dissertation.

Chapter 1

Introduction

1.1 Overview

Reinforced concrete bridge columns typically experience relatively low axial loads, which facilitates detailing for a ductile flexural response where yielding is primarily due to the ductile behavior of the longitudinal reinforcement. In contrast, the arches of reinforced concrete arch bridges can be subjected to axial forces that approach or exceed the balanced axial force. Such high axial forces present challenges in detailing for ductile flexural response, as failure may be dominated by concrete crushing and buckling of the longitudinal reinforcement.

Consequently, designers are increasingly interested in understanding how axial loads impact the performance of reinforced concrete arch bridges, particularly under seismic conditions. The primary concerns are the effects of these axial loads on the arch rib's displacement capacity and cross-sectional damage for different drift levels. Identifying transverse reinforcement details and configurations that provide satisfactory performances or can improve an element displacement capacity under moderate to high axial loads and lateral forces is key to ensuring safe designs that meet local seismic regulations performance targets.

While the California Department of Transportation provides classifications and performance objectives for bridges, none are specifically oriented to arch bridges despite their unique geometry and structural characteristics. The Spanish Creek Replacement Bridge (Bridge No. 09-0077) and the Shasta Viaduct Replacement (Bridge No. 06-0212L) are two examples of reinforced concrete arch bridges constructed in California and served as prototypes for this research program. The Spanish Creek Bridge consisted of a rectangular cross section with rectangular stirrups and cross-ties used to confine the core and restrain the longitudinal bars. The Shasta Viaduct Bridge has a square cross section with a circular confined core, achieved using welded circular hoops as transverse reinforcement.

1.2 Research Objectives and Scope of Work

This dissertation discusses the influence of high axial forces on the structural behavior of reinforced concrete arch bridges. The primary objectives are to evaluate the effectiveness of various confinement reinforcement details in improving displacement capacity, assess the effects of high axial forces on drift capacity, and recommend detailing practices for earthquake-resistant design of arch bridges.

The research includes experimental data from nine 1/3-scale specimens representing the critical region of an arch rib. The collected experimental test data was used to calibrate finite element models and conduct a comprehensive parametric study on critical variables such as confined section geometry, transverse reinforcement detailing, and axial force ratio. Finally, a suggested methodology is presented to examine the dynamic behavior and seismic performance of selected arch rib cross sections.

1.3 Report Organization

Chapter 1 introduces the project's overview, objectives, scope, and research significance.

Chapter 2 presents the procedures and results of an experimental program examining the behavior of reinforced concrete arch ribs under moderate to high axial compressive forces and incremental cyclic lateral loading. Nine 1/3 scale specimens representing the critical region of an arch rib were built and tested. The primary test variables were the confined section geometry, amount of confining reinforcement, spacing of transverse reinforcement, and axial force. Results highlight the importance of confinement reinforcement detailing in maintaining structural integrity under seismic loading. This chapter provides detailed experimental data and analysis for the performance assessment of these test specimens under seismic conditions.

Chapter 3 describes an extensive parametric study on the seismic response of reinforced concrete arch segments. Utilizing OpenSees, a series of analytical fiber models were developed to evaluate the effects of various transverse reinforcement details and axial force ratios on arch rib seismic performance. Experimental data from scaled arch specimens was used to calibrate and validate the models. The validated parametric models provide a robust dataset that complements the experimental findings. The obtained results support the experimental findings: increasing transverse reinforcement enhances deformation capacity, while higher axial force ratios reduce drift ratio capacity.

Chapter 4 introduces a methodology to explore the dynamic behavior of arch rib sections derived from the Shasta Viaduct Replacement Bridge under seismic loading using nonlinear finite element models using OpenSees. The methodology objective is to present a framework to develop an arch bridge risk analysis. Suggested results include the development of fragility functions and engineering demand parameter hazard curves at different damage states. The methodology suggests using Conditional Site Spectra to define a set of hazard-consistent ground motions with assigned occurrence rates.

Chapter 5 summarizes the dissertation and reiterates the conclusions. Based on the experimental and analytical data, it provides design recommendations for reinforced concrete bridge arch ribs.

The appendix material includes photographs from the laboratory tests and extensive information about the test specimen instrumentation and steel reinforcement properties.

Chapter 2

Experimental Tests on Seismic Response of Reinforced Concrete Arch Segments

Authors: Diego De la Mora and Jack P. Moehle

2.1 Abstract

Nine large-scale specimens were constructed to replicate the critical region of a bridge arch rib. Each specimen was subjected to a constant axial force ranging between 16 and 40 percent of the product of the gross cross-sectional area and concrete compressive strength and loaded laterally with increasing reversed cyclic displacement amplitudes until failure. Key test variables included confined section geometry; type, quantity, and spacing of confining reinforcement; and axial force. Confinement details included circular hoops and rectilinear hoops with both hook and double-headed cross-ties. Results indicate that circular hoops enhance ductility capacity compared with rectilinear hoops with hooked cross-ties. Rectilinear hoops with double-headed cross-ties exhibited improved ductility capacity but require rigorous quality control to ensure the heads engage longitudinal reinforcement. Increment in the volume of transverse reinforcement proportionally increases the deformation capacity. Closer transverse reinforcement spacing is crucial for ensuring ductile behavior. High axial force reduces the displacement ductility capacity of the member and produces severe damage in the core at large drifts.

2.2 Introduction

Reinforced concrete arch bridges have large cross sections and are subjected to high axial compressive forces that may reach or exceed the balanced axial force. The relatively high axial force creates challenges in detailing for ductile flexural response because failure can be dominated by crushing of concrete and buckling of longitudinal reinforcement. The capability to experience ductile response without failure can be important for all bridge structures but is especially important in regions subjected to strong earthquakes because fault rupture offsets or shaking can lead to inelastic response in the arch. In contrast, reinforced concrete bridge columns typically have axial forces well below the balanced axial force, which facilitates detailing for ductile flexural response.

Large-scale tests focusing on reinforced concrete bridge arches are scarce. Several studies of reinforced concrete columns under moderate to high axial forces and reversed cyclic lateral displacements have been reported. The configurations of the columns in those tests, however, are generally based on typical building columns, having smaller overall cross sections with smaller number of longitudinal reinforcing bars than is typical of arch bridge segments. Studies done on reinforced concrete bridge columns typically lack high axial forces typical of bridge arches. Studies are needed to define design and detailing requirements for bridge arches located in regions of high seismicity.

Nine one-third-scale specimens were constructed to represent the critical region of a reinforced concrete arch rib. These specimens were tested under constant axial force and reversed, cyclic, lateral displacements of progressively increasing amplitude until failure. The main test parameters are the axial force ratio and the configuration, volumetric confinement ratio, and spacing of the transverse reinforcement.

2.3 Literature Review

Lehman *et al.* [1] tested ten spiral-reinforced bridge columns with circular cross sections. The columns had aspect ratios ranging from 3 to 10. Columns were tested under a constant axial force varying between 0.1 and 0.2 times $A_g f'_c$, where A_g = gross cross-sectional area and f'_c = compressive strength of concrete. A conclusion from this study is that the damage progression was similar for all columns, with initial concrete cracking, followed by yielding of the longitudinal reinforcement, cover spalling, core crushing, longitudinal reinforcement buckling, spiral fracture, and longitudinal reinforcement fracture. Longitudinal bar fracture was attributed to fatigue damage associated with cyclic loading and longitudinal bar buckling. All test columns maintained their axial force capacity through displacement cycles well past the onset of lateral strength decay.

Saatcioglu and Ozcebe [2] reports on tests of fourteen square columns, with five subjected to constant axial compressive force and reversed cyclic lateral displacements. They conclude that the presence of a constant axial force reduces the ductility capacity and accelerates strength degradation. Additionally, they suggest that the use of proper confinement can significantly improve the ductility capacity of columns under the combined effect of axial force and bending moment. Atalay and Penzien [3] studied rectangular building columns. In their tests, columns with aspect ratios exceeding 6 were subjected to moderate and high axial force ratios and reversed cyclic lateral displacements. They concluded that axial force significantly affects the behavior of the column critical region, suggesting extreme care in the design of critical regions with axial force of $0.4 A_g f'_c$ or higher.

Zahn [4] reports tests of fourteen columns. These columns varied between a rectangular cross section and confined core, an octagonal cross section with circular confined core, and hollow circular sections. The applied constant axial force varied from 0.1 to $0.58 A_g f'_c$. Zahn states the importance of closely spaced transverse reinforcement to control the longitudinal reinforcement from buckling and improve arching action of the confined core between adjacent hoops. Regarding the hollow sections, ductile behavior was only found in sections with a ratio of inside to outside diameter less than 0.6 and an axial force less than $0.15 A_g f'_c$. Additionally, Zahn *et al.* [5] concluded that the position of the neutral axis at flexural strength has a strong influence on the column ductility. The main controlling factors in determining the neutral axis position at flexural strength are the axial force ratio, the inside to outside diameter ratio, the longitudinal steel ratio, and the material strengths. Other researchers [6], [7] agree with the importance of the neutral axis location and inside-to-outside diameter ratio in determining ductility capacity for hollow sections.

Different configurations of rectilinear reinforcements, including hoops and crossties, can be used in columns. Where crossties use 90-degree hooks at one end, the opening of the 90-degree hooks has been reported in columns under constant axial force and cyclic lateral displacements [8], [9],

suggesting that a 90-degree hook does not provide effective restraint to prevent buckling on the longitudinal reinforcement. Sheik and Yeh [10] studied fifteen square columns using various crossties configurations. They found that configurations with 90-degree hooks confined the concrete effectively and increased moment capacity at small deformations. However, at larger deformations, the hooks tended to open, leading to brittle failure. They caution against using 90-degree ties in columns under high axial loads.

The use of double-headed crossties as an alternative to hooked crossties has been studied. Youakim and Ghali [11] tested four columns under constant, moderate axial force and increasing lateral displacement cycles. Two of the columns were reinforced using regular alternating 90-degree and 135-degree hooked crossties, and the other two columns had double-headed studs as crossties. It was concluded that the double-head crossties resulted in superior behavior compared with conventional crossties. Ha *et al.* [12] report column tests using crossties with either one head or two heads, concluding that the headed crossties performed similar or superior to the columns with conventional crossties. Crossties with 90-degree hooks opened, allowing longitudinal reinforcement to buckle, while headed crossties were able to delay the buckling of the longitudinal bars.

2.4 Research Significance

Few laboratory experiments previously have demonstrated seismic performance characteristics of reinforced concrete arch bridge segments. This study explores the behavior of scaled model segments subjected to high axial forces, assesses the effectiveness of different confinement reinforcement details, presents novel data, and recommends detailing practices for the earthquake-resistant design of arch bridges.

2.5 Test Specimen Configurations

Two reinforced concrete arch bridges designed and constructed in California by the California Department of Transportation (Caltrans) were selected as prototypes for this study: the Spanish Creek Replacement Bridge and the Shasta Viaduct Replacement Bridge. The Spanish Creek Replacement Bridge arches consisted of a rectangular cross section with rectilinear stirrups and crossties with 90-degree and 135-degree hooks that were alternated around the column perimeter. The Shasta Viaduct Replacement Bridge arches had a square cross section with a circular core confined with circular hoops. This bridge had the main longitudinal reinforcement arranged in a circular pattern with secondary reinforcement, both longitudinal and transverse, placed outside the confined core.

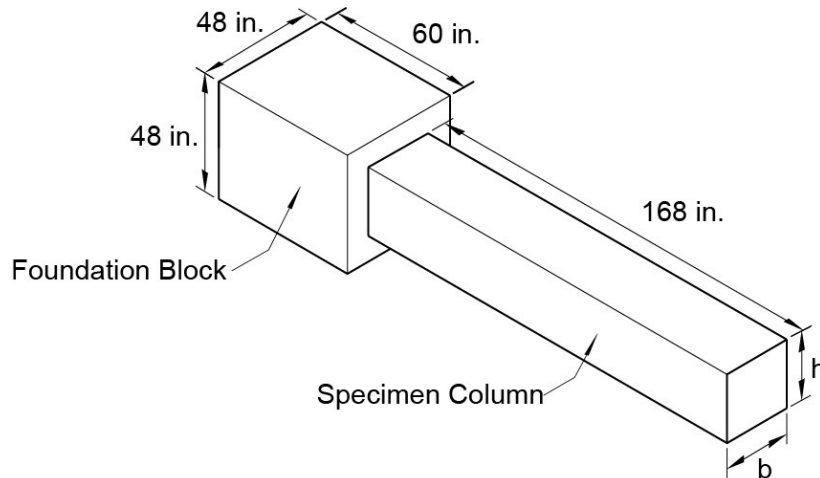


Figure 2.1. General specimen dimensions.

Test specimens were constructed to approximate one-third scale replicas of the prototypes, considering material properties and details of the longitudinal and transverse reinforcement. Each tested specimen consisted in two primary elements: a foundation block and a column, as shown in Figure 2.1. The foundation block, which had the same dimensions for all test specimens, was heavily reinforced to avoid any failures during testing. The column, representing the arch element of the bridge, had a gross cross section with a base, b , and a height, h , as listed in Table 2.1 All cross sections, except Specimen 1 and 2, had a 34.9 mm (1-3/8 in) chamfer at each of four corners, scaled from chamfers in the prototypes. In addition to the column cross-sectional dimensions, the primary column variables were axial force ratio and confinement reinforcement configuration, volume ratio, and longitudinal spacing.

The axial force ratio applied to a test column is defined as $P/A_g f'_c$, where P denotes the constant axial force applied during a test, A_g is the gross cross-sectional area of the column, and f'_c is the concrete compressive strength measured from concrete cylinders on the day of testing. Table 1 lists values of $P/A_g f'_c$.

Three different configurations of transverse reinforcement were used, as shown in Table 1. The first configuration, used for Specimens 1 and 2, followed the Spanish Creek Bridge prototype, with square hoops and alternating crossties. The second configuration, used for Specimens 3 through 7, followed the Shasta Viaduct Bridge prototype, with circular hoops to define the section core and secondary reinforcement cast in a square shape around the circular core. The third confinement configuration, used for Specimens 8 and 9, consisted of square hoops and double-headed bars as crossties.

The volumetric confinement ratio, denoted as ρ_c , is the volume ratio of transverse confinement reinforcement with respect to the confined core measured to the outside of the transverse reinforcement. For rectangular confined sections it can be computed using Equation (2.1) where $\sum A_{sx}$ and $\sum A_{sy}$ are the total areas of each hoop set in the directions parallel to b_c or h_c , s is the longitudinal spacing between hoop sets, and h_c or b_c is the confined core height or width measured out-to-out of the perimeter hoop. These transverse reinforcement ratios in each direction can be

rewritten as ρ_{tx} and ρ_{ty} . Equation (2.2) can be used to obtain the volumetric confinement ratio for sections with a circular confined core. Here, A_{sh} is the circular hoop bar area, s is the longitudinal spacing between hoops, and d_c is the circular confined core diameter measured to the outside of the hoops.

$$\rho_c = \rho_{tx} + \rho_{ty} = \frac{\sum A_{sx}}{s h_c} + \frac{\sum A_{sy}}{s b_c} \quad (2.1)$$

$$\rho_c = \frac{4A_{sh}}{s d_c} \quad (2.2)$$

Table 2.1 summarizes details for each of the nine test specimens, including cross-sectional configuration; length-to-depth aspect ratio; measured concrete compressive strength on the day of testing, f'_c ; volumetric confinement ratio, ρ_c ; the transverse reinforcement bar size and longitudinal spacing, s ; longitudinal reinforcement diameter, d_b ; ratio s/d_b , longitudinal steel ratio, ρ_l ; applied axial force, P ; and axial force ratio $P/A_g f'_c$.

Specimens 1 and 2 had a rectangular core confined with rectilinear stirrups and crossties. The vertical direction confinement consisted of stirrups with a cap-tie forming a perimeter “hoop” with additional crossties to restrain the longitudinal bars. The stirrups terminate in 135-degree hooks, and the crossties in 135-degree and 90-degree hooks. In the horizontal direction, crossties in alternating order were placed. All 135-degree hooks engage the longitudinal bars and perimeter hoop. Specimens 1 and 2 had values of $P/A_g f'_c = 0.25$ and 0.40 , respectively. Specimens 3 to 6 had a rectangular cross section with a confined core with butt-welded circular hoops and primary longitudinal reinforcement placed inside the circular hoops. Secondary U-shaped, rectilinear hoops were lap-spliced to provide a continuous hoop to contain the corners of the cross sections with No. 4 longitudinal bars. Axial force ratio and transverse reinforcement ratio and spacing were varied. Specimen 7 was similar to Specimen 6 but included a hollow section with a 406 mm (16 inch) diameter steel pipe at the center. The inner void diameter to outside diameter ratio, D_i/D , for this section is 0.6, Zahn *et al.* [5] suggests that this ratio is not bigger than 0.7, in order to obtain a ductile behavior. The axial force ratio for this specimen was selected so that the neutral axis depth at flexure is the same as in Specimen 6. Zahn *et al.* also suggests that, to have a ductile behavior, the neutral axis should be located outside the void. In this specimen, the neutral axis was located inside the void section. The pipe, 6mm (1/4 inch) thick ASTM A500 Grade C, extended approximately 13 mm (1/2 inch) into the foundation block, with the intent that it would resist inward dilation of the core concrete without substantially contributing to moment resistance. Specimens 8 and 9 consisted of square confined cores with rectilinear perimeter hoops and double-headed crossties. The crossties comprised 32 mm (1.25 inch) square heads welded to 10 mm (No. 3) bars, resulting in a bearing area equal to $14A_b$, where A_b is the reinforcement bar area.

2.6 Materials

All specimens were cast in a horizontal position using a similar normal-weight concrete mix, with a 28-day target strength of 27.5 MPa (4000 psi) and a maximum aggregate size of 10 mm (3/8 inch). 150 mm by 300 mm (6 inch by 12 inch) companion cylinders cured alongside the test specimens were tested to gauge the compressive strength and stress-strain relationship at the day of testing. Mean strain at the peak of the concrete stress-strain relationship was 0.0033.

Longitudinal and transverse reinforcement was specified to meet the ASTM A706 Grade 420 (60) specifications except for the 6mm (No. 2) wire used for the crossties. 16 mm diameter (No. 5) bars were used as longitudinal reinforcement in all specimens, with Specimen 1 and 2 also having 13 mm diameter (No. 4) bars as longitudinal reinforcement. Specimen 3 to 7 was also reinforced with 9.5 mm diameter (No.3) bars outside the confined core. The foundation block was heavily reinforced with a grid of 32 mm diameter (No. 10) headed bars and 13 mm (No. 4 bars) bent bars. The stress-strain relationships for the principal longitudinal bars used in the specimens are shown in Figure 2.2a. The stress-strain relationship for the transverse reinforcement and steel pipe are shown in Figure 2b. A table containing the full measured reinforcing steel properties is shown in Appendix B.

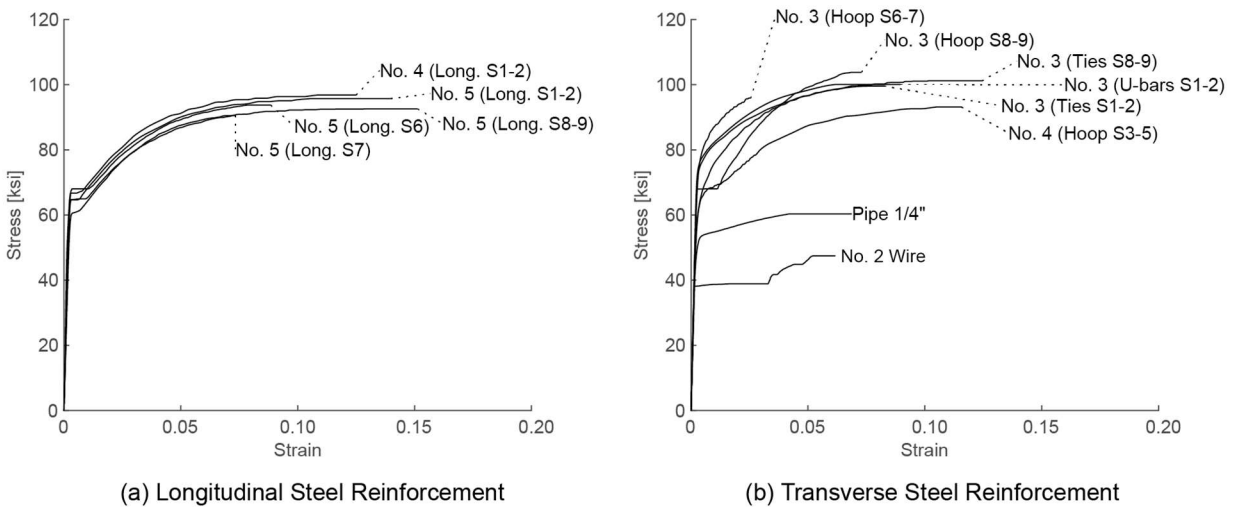
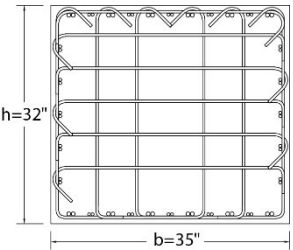
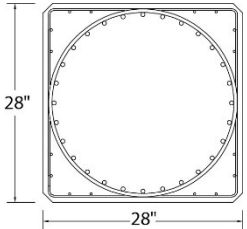
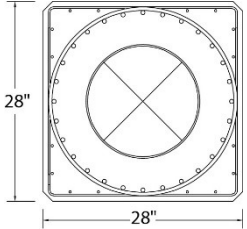
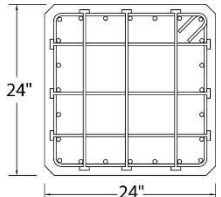


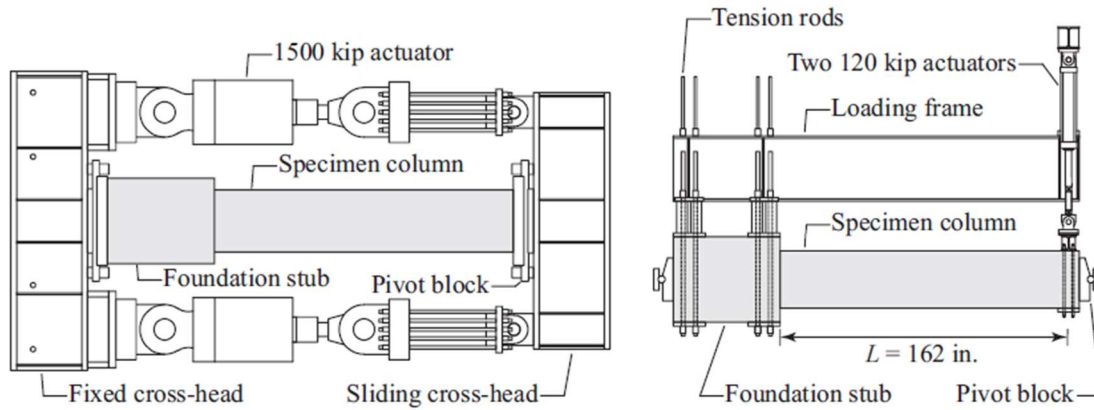
Figure 2.2. Stress-Strain relationships of the reinforcing steel used in tests.

Table 2.1. Properties and details of test specimen

Specimen	Cross Section	Aspect Ratio	f'_c , MPa [ksi]	Concrete Elastic Modulus, E , Mpa x10 ³ [ksi x10 ³]	Transverse Reinf. Bar size	ρ_c	s , mm [in]	Long. Bar Diameter, mm	s/d_b	ρ_l	P, kN [kips]	$P/A_g f'_c$
1		5.07	31.1 [4.51]	18.6 [2.70]	No. 3	0.015	76.2 [3]	16 (No. 5)	4.8	0.014	6010 [1350]	0.25
2		5.07	40.0 [5.80]	19.9 [2.88]	No. 3	0.015	76.2 [3]	16 (No. 5)	4.8	0.014	11500 [2590]	0.40
3		5.78	34.5 [5.01]	17.6 [2.55]	No. 4	0.008	101.6 [4]	16 (No. 5)	6.4	0.011	4340 [975]	0.25
4		5.78	39.4 [5.71]	19.1 [2.78]	No. 4	0.015	50.8 [2]	16 (No. 5)	3.2	0.011	4870 [1100]	0.25
5		5.78	33.0 [4.79]	20.0 [2.90]	No. 4	0.015	50.8 [2]	16 (No. 5)	3.2	0.011	6650 [1500]	0.40
6		5.78	29.9 [4.34]	19.3 [2.81]	No. 3	0.008	50.8 [2]	16 (No. 5)	3.2	0.011	3780 [850]	0.25
7		5.78 5.78	29.4 [4.26]	20.4 [2.96]	No.3	0.008	50.8 [2]	16 (No. 5)	3.2	0.011	2450 [550]	0.16
8		6.75	33.1 [4.80]	21.0 [3.05]	No.3	0.024	50.8 [2]	16 (No. 5)	3.2	0.013	3020 [680]	0.25
9		6.75	33.1 [4.80]	21.2 [3.07]	No.3	0.016	76.2 [3]	16 (No. 5)	4.8	0.013	3020 [680]	0.25

2.7 Testing

The test setup is composed of two loading frames, an axial load frame to apply axial force (Figure 2.3a) and a lateral load frame to apply lateral forces to the specimen (Figure 2.3b).



(a) Plan view. Axial load frame.

(b) Elevation view. Lateral load frame.

Figure 2.3. Loading frame configuration. (Miller [13]).

For the axial load frame, two crosshead beams were positioned at the ends of the specimen and were connected using two 6.7×10^3 kN (1500 kip) capacity hydraulic actuators. The specimen is attached at both ends to steel pivot blocks that support the specimen self-weight and allow rotation at the specimen ends. The crosshead on the foundation side is fixed to the laboratory strong floor to prevent translation, while the crosshead at the tip rests on a rail system that permits horizontal translation without vertical movement. Hydraulic actuators control axial force P (Figure 2.4) under displacement control, ensuring parallel crosshead movement.

The second frame is formed by a steel beam fixed to the foundation block with high-strength steel rods and connected near the specimen tip through two 533 kN (120 kip) capacity actuators. The actuator displacement induces shear and bending moment in the specimen. When the actuators extend, they produce flexure in the column with flexural tension on the top surface and compression on the bottom surface. The actuators produce lateral cyclic force V applied 4.11 m (162 inches) from the column-foundation joint interface (Figure 2.4).

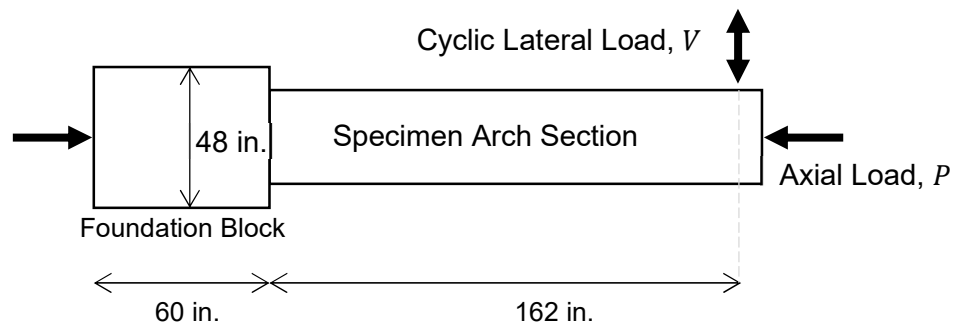


Figure 2.4. Forces applied in the specimen during testing.

The photograph in Figure 2.5 shows a test specimen in the loading frames.



Figure 2.5. Global view of test specimen during testing.

The test protocol begins with application of the assigned constant axial compressive force P indicated in Table 2, which is maintained throughout a test. The lateral displacement protocol follows FEMA 461 guidelines [14], applying cyclic lateral displacement with progressively increasing target displacements. Specimens 1 to 7 had two displacement cycles per displacement step, while Specimens 8 and 9 experienced three cycles per displacement step. The amplitude increment at each displacement step was 1.4 times the amplitude of the preceding step (except for Specimen 1 and 3, where the amplitude increment factor was 1.5). The initial target displacement was selected such that three to four amplitude steps were completed before reaching the effective yield point of the critical section.

2.8 Instrumentation

Instrumentation for global response measurements included load cells to measure applied axial and lateral forces and string potentiometers to measure global displacements and rotations of the foundation block and the column tip (the point where the vertical force was applied) at each side of the test specimen. Column tip displacement Δ_t is reported as a displacement relative to a tangent drawn to the foundation block (Figure 2.6). Appendix B provides a thorough description of the instrumentation employed during the experimental program.

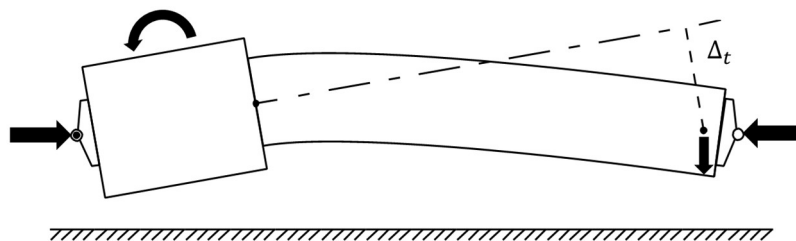


Figure 2.6. Specimen deformed shape during testing.

A truss arrangement of Linear Variable Differential Transformers (LVDTs) was placed on one lateral face of the column from the column-foundation joint to two section depths away, with four bays in total (Figure 2.7). The LVDTs were attached to anchor rods that were cast inside the column core. The instruments measured relative displacement between the anchor rods, from which a discrete average strain profile can be obtained. Fiber Optics were implemented in the last four specimens enabling the measurement of continuous strain profiles along the column full length. Results obtained from the fiber optics data can be found in Liu *et al.* [15].

Longitudinal and transverse reinforcement had strain gauges at discrete locations within a length commencing inside the foundation block and extending twice the section depth along the column length. The steel pipe of Specimen 7 was instrumented with strain gauges at the top and bottom face, spaced every sixteen inches (same as the pipe diameter) starting at the foundation block-column joint.

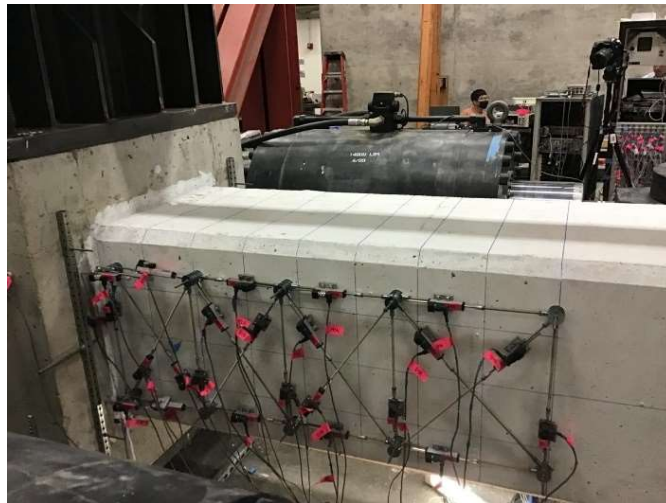


Figure 2.7. Instrumentation photograph. Linear potentiometers on south face.

2.9 Test Observations

Typical damage progression started with flexural cracks forming close to the column-foundation joint at a drift ratio between 0.5% and 1.0%. Subsequently, yielding of the longitudinal reinforcement occurred at approximately 1.1% drift ratio for circular confined specimens and 1.8% drift ratio for specimens with rectilinear reinforcement. Reinforcement yielding typically was followed by cover concrete spalling, with increased loss of cover concrete as the test progressed. Longitudinal bar buckling and fracture were observed close to the column-foundation joint in all tests. In Specimens 5, 6, and 7, fracture of the main transverse reinforcement was observed.

The damage within the critical section adjacent to the foundation block varied based on the transverse reinforcement detailing and axial force ratio. Specimens 1 and 2, featuring rectangular confined cores with crossties having 135-degree and 90-degree hooks, experienced significant damage and concrete degradation. Crosstie hooks began to open, leading to extensive buckling of longitudinal bars, concrete crushing, and expulsion of core concrete. Specimen 2, subjected to higher axial force, exhibited more notable concrete core degradation. Longitudinal bar buckling

and fracture, combined with crushing of the concrete confined core, led to failure of both sections. Figure 2.8a and b show photographs of the damage sections taken after the test protocol was completed.

Specimen 3, which had the circular confined core with circular hoops at spacing equal to $6.4d_b$, sustained extensive longitudinal bar buckling, possibly attributable to the relatively large s/d_b ratio. Bar buckling was also associated with localized crushing of the concrete core. As the loading cycles continued, the localized damage worsened (Figure 2.8c), including fracture of longitudinal bars, which contributed to a rapid loss of lateral force capacity.

Specimen 4 had half the transverse reinforcement spacing s and twice the hoop volumetric ratio ρ_c compared with Specimen 3. The concrete core appeared to be relatively undamaged throughout the duration of the test (Figure 2.8d). Nonetheless, at large displacements the longitudinal reinforcement fractured, leading to strength degradation.

Specimen 5 was nominally identical to Specimen 4 except it was tested under higher axial force ratio. Main longitudinal reinforcement buckled in the spacing between hoops and concrete crushing extended into the confined core. In the final cycles, longitudinal and transverse reinforcement fractured, leading to increased damage of the core concrete. At zero displacement, while holding the axial force constant, several circular hoops fractured sequentially, leading to axial collapse of the test specimen near the foundation block (Figure 2.8e). Testing was stopped after this failure.

Specimen 6 had a volumetric confinement ratio equal to that of Specimen 3, achieved with a reduced hoop spacing and reduced transverse reinforcement bar size. The smaller spacing between the hoops provided better support to the longitudinal bars, producing a similar failure progression as Specimen 4, showing almost no damage in the core material (Figure 2.8f). This specimen was able to sustain higher displacement amplitudes than Specimen 3.

Specimen 7 had a hollow cross section formed by a steel pipe. The axial force ratio had been selected such that the theoretical location of the neutral axis for Specimen 7 would be the same as the neutral axis location for Specimen 6 near flexural strength. Specimen 7 exhibited behavior like Specimen 6. After the initiation of concrete spalling, the secondary longitudinal bars buckled followed by buckling of the main longitudinal reinforcement. Almost half of the longitudinal reinforcement and three hoops were fractured during testing. At the later loading stages (Figure 2.8g), the core material was severely crushed, exposing the steel pipe. The apparent damage was accompanied by a loss in lateral resistance of the element. Strain gauges on the steel pipe showed maximum strain of $\varepsilon = 0.0013$ in tension, and $\varepsilon = 0.0015$ compression. Visual inspection after the test showed that the steel pipe had buckled at the column-foundation joint.

In sections with circular confined cores, the spalling of the cover concrete led to the detachment of substantial cover material, mainly from the test specimen unconfined corners. As spalling of cover material spread along the sides of the cross section, the lap splice of the secondary transverse U-bar ties failed leading to opening of the ties. Consequently, the sacrificial cover surrounding the circular core spalled completely and fell away, leaving a relatively short length of the confined circular core exposed. This failure may have somewhat constrained the length of the plastic region.

Specimen 8 and 9 had flexural cracks and concrete cover spalling spread over a longer length in comparison with previous tests in this series. Specimen 8 had bar buckling in five longitudinal bars and one fractured bar. It was observed in one location that if a headed bar was not properly placed and did not provide restraint to the adjacent stirrup, the stirrup and longitudinal bar bulged. The test was ended because the test apparatus reached its displacement limit. No apparent damage was visible in the confined section. Specimen 9 showed more damage in the longitudinal reinforcement, with several longitudinal bars buckling. In the final cycles, longitudinal bars started to fracture. Like Specimen 8, the material in the confined core had no visible damage at the end of the test. None of the headed bars sustained fractures in the heads or the bars.

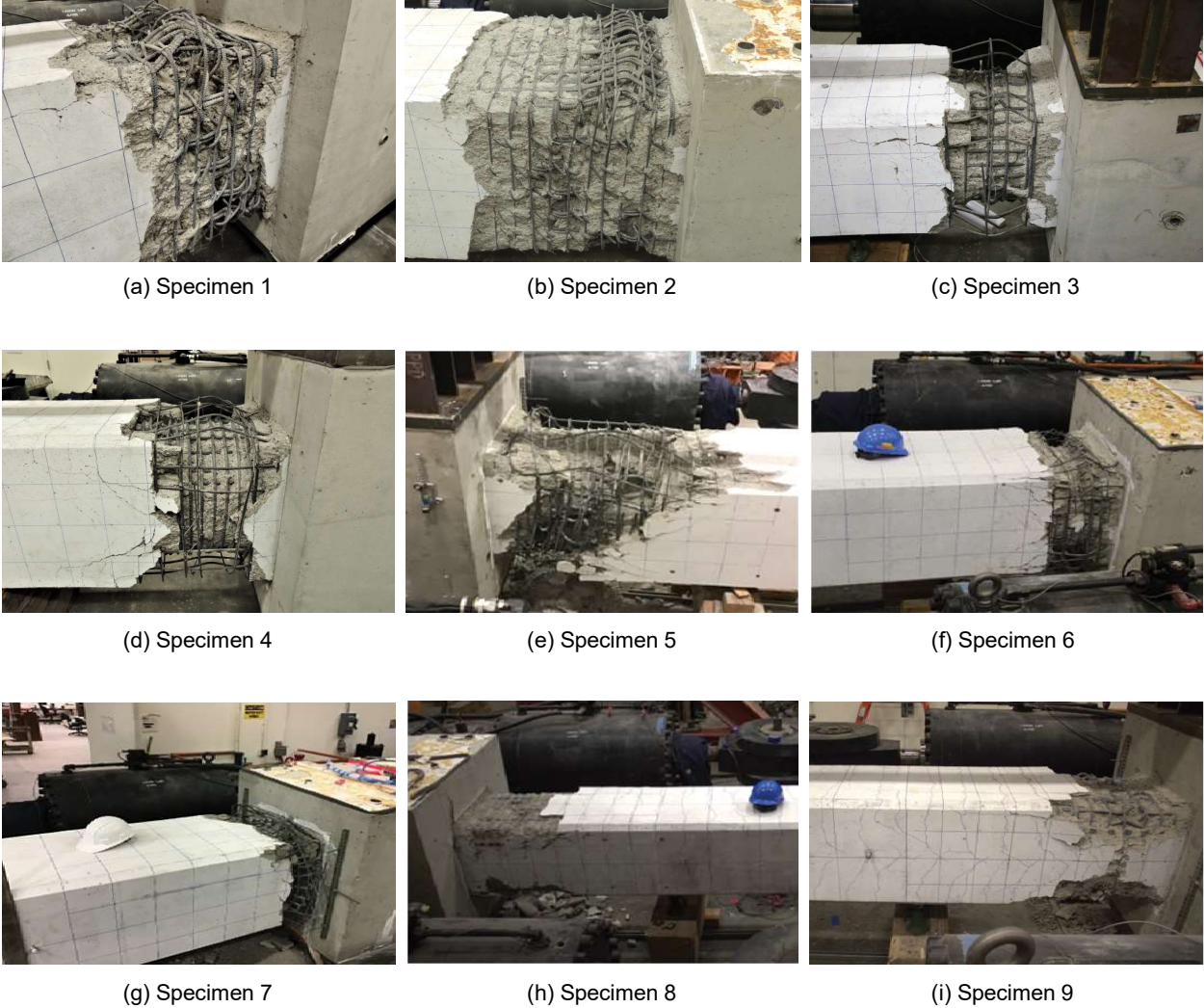


Figure 2.8. Post test photographs.

2.10 Overall Measured Results

It is of interest to compare the global moment-displacement relationships obtained during the tests along with stiffness, strength, and deformation capacity indices. First, it is necessary to define conditions of equilibrium, deformations, and the various indices of interest.

Figure 2.6 illustrates the deformed specimen shape during testing. Axial shortening occurs in the column and the foundation block due to axial compressive loading. Lateral deformation occurs due to column flexure, column shear, and rigid-body rotation due to rotation of the foundation block and slip of the longitudinal reinforcement from the foundation block. We define effective column lateral deformation Δ_t as the total lateral deformation of the column relative to a tangent drawn to the foundation block – this deformation excludes the effect of rigid-body rotation of the foundation block. Lateral drift ratio is defined as the displacement Δ_t divided by the length from the face of the foundation block to the location of applied lateral force V .

The lateral loading V applied near the end of the column produces an approximately linear moment profile along the column, having the maximum value at the interface between the column and the foundation block. The exact moment profile was calculated using equilibrium in the deformed specimen geometry including self-weight of the test specimen and loading apparatus. Details of the displacement and equilibrium calculations are described by Miller [13]. In the present paper, the term moment refers to the moment calculated at the base section of the column with axial force assumed to act at the geometric centroid of that section.

Moment-drift ratio backbone curves were determined according to ASCE 41-17 [16] for both loading directions. For a given absolute value of drift ratio for loading in opposite directions, the absolute values of the moments were averaged and then normalized by the maximum average moment. The measured relationship between the normalized moment at the column-joint intersection and lateral drift ratio and average backbone curves are plotted in Figure 2.9. The drift ratio, in percentage, is marked on the primary X-axis. A secondary X-axis, provided at the top of each graph, denotes the specimen displacement ductility, that is, the instantaneous lateral displacement divided by the yield displacement Δ_y (see next paragraph). The primary Y-axis represents the bending moment at the column base assuming the axial force acts at the geometric centroid of the column cross section, normalized by the maximum moment of the average backbone curve, M_{max} . A secondary vertical axis denotes the magnitude of the bending moment in kip-ft.

The moment-drift ratio plots of Figure 2.9 show characteristics typical of slender, ductile reinforced concrete components, that is, an initially stiff response prior to the onset of cracking, reduced stiffness after onset of cracking, apparent yielding at drift ration on the order of 0.01, a spindle-shaped moment-deformation relationship after yielding, and varying degrees of strength decay after yielding dependent apparently on the configuration of the cross section and the axial load ratio.

The procedure described by Elwood and Eberhard [17] was followed to determine an effective stiffness, EI_{eff} , and effective yield displacement, Δ_y for each test specimen. For this purpose, a moment-curvature analysis was done to determine the effective strength $M_{0.004}$, that is, the theoretical moment at the column critical section when the extreme concrete fiber reaches a maximum compressive strain of 0.004. A first yield point was defined as the moment in the moment-curvature relationship at which the tension reinforcement yields, or the maximum compressive concrete strain reaches 0.002, whichever occurs first. Then a secant was drawn from

the origin through the bending moment at first yield on the averaged moment-drift ratio backbone up to the intersection with $M_{0.004}$. The intersection defines the effective yield displacement, Δ_y .

The moment-curvature analysis used the measured steel tensile properties adjusting the post-yield buckling behavior following the method proposed by Dhakal *et al.* [18]. The confined core concrete and unconfined cover concrete stress-strain relationships were modeled according to Mander *et al.* [19]. For this analysis, it was assumed that plane sections remain plane.

The maximum applied moment on the cross section, M_{max} , corresponds to the maximum moment of the averaged backbone. The value of M_{max} is heavily dependent on the amount of cover concrete in the cross section. Specimens 3 to 7 with a circular confined core have a ratio of the confined core to gross area $A_c/A_g = 0.70$, whereas specimens with a rectangular confined core have a ratio of the confined core to gross area $A_c/A_g = 0.94$ for specimens 1 and 2, and $A_c/A_g = 0.88$ for specimens 8 and 9. The concrete cover contributes to produce an initial moment capacity greater than the capacity that can be provided by the confined core. Spalling of the cover results in loss of moment resistance, which tends to decay to a value that can be provided by the confined core only, with greater strength decay apparent for columns with smaller values of A_c/A_g , that is, Specimens 3 through 7. Specimens 1 and 2 show strength decay partly due to loss of cover concrete, but also because the core is less well confined by the rectilinear transverse reinforcement and begins to decay shortly after yielding. Specimens 8 and 9 strain-harden after yielding, apparently because of the small cover combined with the effective confinement reinforcement.

Ultimate displacement, Δ_{80} , is defined as the displacement at the moment resistance of the average backbone curve decays to 80% of the maximum moment M_{max} . Specimen 8 did not experience a 20% decrease in moment resistance during the test, due to limitations on the test apparatus, and therefore the largest equivalent tip displacement recorded is used as Δ_{80} for this case. For all the other specimens, testing continued until visible failure of the cross section beyond Δ_{80} .

Figure 2.9 identifies the occurrence of two damage states observed during the test, cover spalling and first bar fracture. A red diamond marks the moment where the cracked column cover started to spall, typically close to the foundation block, while a red star marks the point where a longitudinal bar fracture was observed. The effective yield displacement, Δ_y , and ultimate displacement, Δ_{80} , are marked using a yellow circle and triangle, respectively.

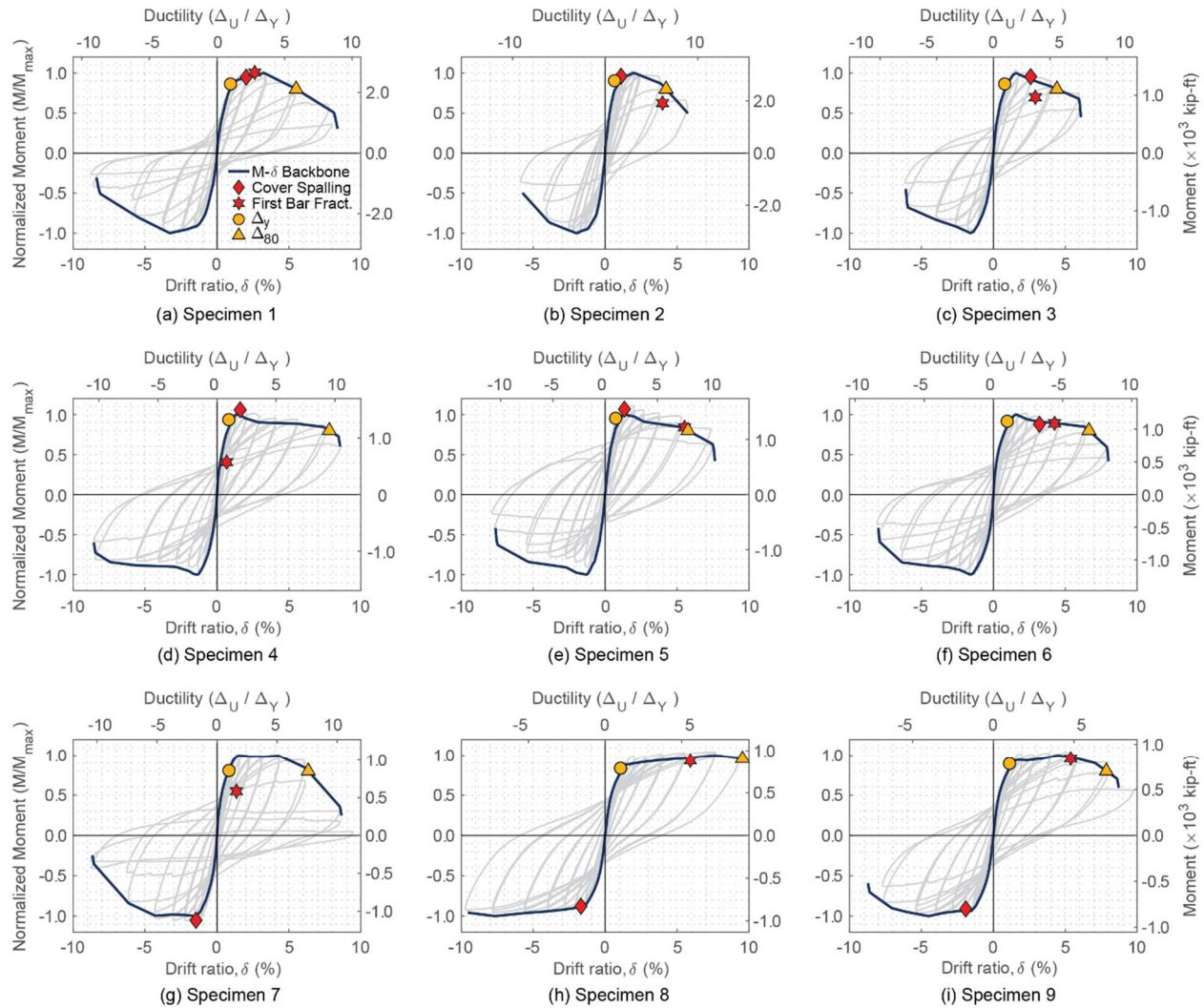


Figure 2.9. Specimens Moment-Drift relationship.

Table 2.2 presents values of M_{max} , $M_{0.004}$, and the ratio between $M_{0.004}$ and M_{max} . Drift ratios for effective yield displacement and ultimate displacement are lower for specimens under higher axial forces or with lower transverse confinement. Additionally, Table 2.2 presents the displacement ductility for each specimen, which is the ratio of the effective yield displacement Δ_y over the ultimate displacement Δ_{80} . A key damage state, such as the maximum drift achieved by a specimen before presenting bar fracture is also indicated. The last two columns provide the measured effective stiffness of the columns and the flexural stiffness according to ASCE 41-17, expressed as a fraction of the gross-section stiffness, EI_{eff}/EI_{Gross} , and EI_{ASCE41}/EI_{Gross} , respectively.

Table 2.2. Experimental results summary.

Specimen	M_{max} , kN-m x10 ³ [kip-ft x10 ³]	$M_{0.004}$, kN-m x10 ³ [kip-ft x10 ³]	$M_{0.004}/$ M_{max}	Drift Ratio (%) at Δ_y	Drift Ratio (%) at Δ_{80}	Max Drift Ratio (%) before bar fracture	Displacement Ductility, $\Delta_{80}/\Delta_{\psi}$	$EI_{Eff}/$ EI_{Gross}	EI_{ASCE41} $/ EI_{Gross}$
1	3.58 [2.64]	3.23 [2.39]	0.90	0.94	5.51	8.37	5.86	0.64	0.45
2	4.15 [3.06]	4.00 [2.95]	0.96	0.64	4.23	5.74	6.57	1.08	0.60
3	1.87 [1.38]	1.69 [1.25]	0.90	0.79	4.41	6.08	5.60	0.78	0.45
4	1.91 [1.41]	1.87 [1.38]	0.98	0.82	7.81	8.56	9.51	0.77	0.45
5	1.97 [1.45]	1.92 [1.42]	0.97	0.73	5.76	7.63	7.92	0.85	0.60
6	1.66 [1.22]	1.61 [1.18]	0.97	0.96	6.64	8.00	6.90	0.55	0.45
7	1.44 [1.06]	1.28 [0.94]	0.89	0.84	6.35	8.66	7.60	0.48	0.36
8	1.27 [0.94]	1.12 [0.83]	0.88	1.07	9.54 ^a	9.54	8.96	0.60	0.45
9	1.19 [0.88]	1.11 [0.82]	0.94	1.12	7.86	8.71	7.00	0.56	0.45

^a Specimen 8 test was ended before reaching Δ_{80} , last displacement cycle is reported instead.

2.11 Discussion

For all cases, after the longitudinal reinforcement fractured, the loss in capacity of the specimens started to increase at a higher rate than in previous cycles. The maximum drift ratio achieved before bar fracture was lower for the specimens with high axial force, compared to the specimens with moderate axial force. The only exception is Specimen 3, which presented bar fracture at a drift lower than any other specimen. This column had a s/d_b ratio of 6, this large transverse reinforcement spacing allowed premature bar buckling and eventual bar fracture. Specimens with moderate axial load that had an s/d_b ratio lower than 6 presented bar fracture after higher drift ratios (8 to 9%). Specimen 8, that had the highest volumetric confinement ratio, was able to reach a drift displacement of 9.54% before presenting longitudinal bar fracture. In all cases, bar fracture presented after the ultimate displacement Δ_{80} was reached.

Figure 2.10 maps the experimental data for the nine test specimens. The horizontal axis plots the transverse reinforcement ratio, ρ_c , while the vertical axis shows the drift ratio at the ultimate displacement Δ_{80} . Specimens with similar configurations are represented using a common symbol color. Specimens 1 and 2, with rectangular core, confined with rectilinear stirrups and crossties, are shown in blue; Specimens 3 to 6, with circular hoops and a circular confined core are in green; Specimen 7 with a circular core and hollow section is shown in yellow; and Specimen 8 and 9 with square confined cores using rectilinear perimeter hoops and double-headed crossties are shown in red. Each bubble is labeled next to it with the Specimen number. The bubble areas are proportional to the axial load ratio of said specimen.

From Figure 2.10 some observations can be drawn. (1) For any given geometry increasing the axial force decreases drift ratio capacity. See Specimen 1 against Specimen 2, and Specimen 4

versus Specimen 5. (2) Circular hoops outperform, in terms of drift capacity, rectilinear hoops for any given axial load ratio and transverse reinforcement spacing, e.g., Specimen 1 versus Specimen 4, and Specimen 2 versus Specimen 5. (3) For a given circular hoop reinforcement quantity and axial load ratio, closer spacing works better than wider spacing, Specimen 6 versus Specimen 3. (4) The presence of a void reinforced with a pipe does not significantly affect performance for a given circular hoop reinforcement quantity, spacing, and neutral axis depth (e.g., Specimen 6 vs. Specimen 7), at least for the design criteria employed in the design of Specimen 7. (5) Circular hoops and headed crossies, with spacing close enough to adequately restrain longitudinal bar buckling ($3.2d_b$ and $4.8d_b$) performs equally well, achieving similar drift ratios. These specimens showed a desirable ductile behavior that was not present in the specimens with hooked crossies, regardless of the applied axial force ratio. (6) The longitudinal bar unsupported length ratio, s/d_b , does not significantly impact performance until a critical threshold is reached, for this set of experiments, an upper threshold of $s/d_b = 4.8$ was appropriate to obtain a ductile behavior. (7) Increasing the volume of circular or headed crossie transverse reinforcement, with well-restrained longitudinal bars, produces an increase in deformation capacity (as indicated by the dashed line). However, the drift ratio increase is not linearly proportional with the volume ratio of the transverse reinforcement. Rather, for the range studied, doubling the volumetric confinement ratio produced only a 20% increase in drift capacity. Note that Specimen 8 had only one longitudinal bar fracture before reaching the maximum displacement capacity of the test apparatus and did not reach a 20% loss in M_{max} by the end of testing. Consequently, it is plausible that Specimen 8 might have achieved greater displacement capacity than indicated by the plotted data point in Figure 2.10.

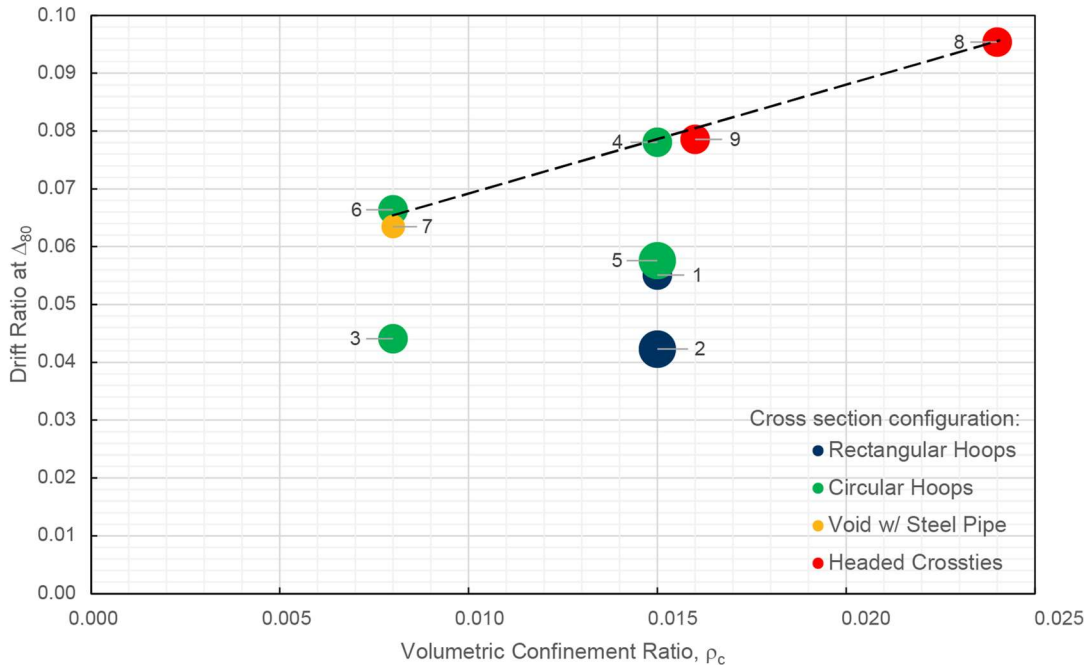


Figure 2.10. Volumetric confinement Ratio - Drift Ratio Relationship.

2.12 Conclusions

Damage progression was similar across all columns. With initial cracking, followed by yielding of the longitudinal reinforcement, cover spalling, longitudinal bar buckling, transverse bar fracture in some cases and longitudinal reinforcement fracture. Note that this follows the damage progression described by Lehman *et al.* [1].

From the experimental data, it can be concluded that increasing axial force reduces drift ratio capacity. Circular hoops outperform rectilinear hoops in terms of drift capacity for the same axial load ratio and spacing. Closer transverse reinforcement spacing enhances drift capacity. Circular hoops and headed cross-ties with adequate spacing ($3.2d_b$ and $4.8d_b$) perform equally well. Longitudinal bar buckling restraint ratios, s/d_b , higher than 4.8 do not provide desirable ductile behavior. Increasing the volume of transverse reinforcement increased deformation capacity, but the increase was not proportional to the volume ratio. The presence of a void reinforced with a pipe with a D_i/D ratio of 0.6 does not significantly affect performance as long as the volumetric confinement ratio, the unrestrained longitudinal bar ratio, and the neutral axis depth at flexure are the same as in a section without a void.

The use of headed bars as cross-ties was an effective method to restrain longitudinal reinforcement. Additionally, the use of headed bars facilitated faster and easier construction. Strict quality control during construction is required, however, because failure to properly engage the heads with the supported longitudinal and hoop reinforcement can result in localized failures that can inhibit overall deformation capacity, future work could explore the use of J-bars as a cross-tie alternative to the double headed cross-ties.

2.13 Bibliography

- [1] D. Lehman, J. Moehle, S. Mahin, A. Calderone, and L. Henry, "Experimental Evaluation of the Seismic Performance of Reinforced Concrete Bridge Columns," *Journal of Structural Engineering*, vol. 130, no. 6, pp. 869–879, Jun. 2004, doi: 10.1061/(ASCE)0733-9445(2004)130:6(869).
- [2] M. Saatcioglu and G. Ozcebe, "Response of Reinforced Concrete Columns to Simulated Seismic Loading," *SJ*, vol. 86, no. 1, pp. 3–12, Jan. 1989, doi: 10.14359/2607.
- [3] M. B. Atalay and J. Penzien, "The seismic behavior of critical regions of reinforced concrete components as influenced by moment, shear and axial force.," *Berkeley: Earthquake Engineering Research Center, University of California*, p. 235, 1975.
- [4] F. A. Zahn, "Design of reinforced concrete bridge columns for strength and ductility.," 1985., [Online]. Available: <http://hdl.handle.net/10092/2872>
- [5] F. A. Zahn, R. Park, and M. J. N. Priestley, "Flexural Strength and Ductility of Circular Hollow Reinforced Concrete Columns without Confinement on Inside Face," *SJ*, vol. 87, no. 2, pp. 156–166, Mar. 1990, doi: 10.14359/9295.
- [6] J. Hoshikuma and M. Priestley, "Flexural behavior of circular hollow columns with a single layer of reinforcement under seismic loading," Jan. 2000.
- [7] X. Liang, "Confined concrete behavior in hollow columns", [Online]. Available: <https://dr.lib.iastate.edu/handle/20.500.12876/28771>

- [8] H. Tanaka, R. Park, and B. Mcnamee, “Anchorage of transverse reinforcement in rectangular reinforced concrete columns in seismic design,” *Bulletin of the New Zealand Society for Earthquake Engineering*, vol. 18, Jun. 1985, doi: 10.5459/bnzsee.18.2.165-190.
- [9] J. C. M. HO and H. J. PAM, “Influence of Transverse Steel Configuration on Post-elastic Behaviour of High-strength Reinforced Concrete Columns,” *HKIE Transactions*, vol. 10, no. 2, pp. 1–9, Jan. 2003, doi: 10.1080/1023697X.2003.10667903.
- [10] S. A. Sheikh and C.-C. Yeh, “Tied Concrete Columns under Axial Load and Flexure,” *Journal of Structural Engineering*, vol. 116, no. 10, pp. 2780–2800, Oct. 1990, doi: 10.1061/(ASCE)0733-9445(1990)116:10(2780).
- [11] S. A. Youakim and A. Ghali, “Ductility of Concrete Columns with Double-Head Studs,” *SJ*, vol. 99, no. 4, pp. 480–487, Jul. 2002, doi: 10.14359/12117.
- [12] T. Ha, S. Lee, and S.-C. Chun, “Cyclic testing of reinforced concrete columns with double or one-side headed shear reinforcement,” *Journal of Vibroengineering*, vol. 18, pp. 4563–4573, Nov. 2016, doi: 10.21595/jve.2016.17421.
- [13] D. J. Miller, “Ductile Behavior of Reinforced Concrete Arch Ribs,” UC Berkeley, 2019.
- [14] FEMA, *Interim protocols for determining seismic performance characteristics of structural and nonstructural components through laboratory testing: FEMA 461*. FEMA, Tech. Rep., 2007.
- [15] H. Liu, D. De la Mora, J. P. Moehle, and M. J. DeJong, “Distributed Fiber-Optic Sensing of Reinforced Concrete Arch Ribs to Monitor Plastic Hinge Formation,” *Structural Health Monitoring*, no. [Submitted for publication.].
- [16] ASCE/SEI 41-17, *Seismic Evaluation and Retrofit of Existing Buildings*. American Society of Civil Engineers, 2017. doi: 10.1061/9780784414859.
- [17] K. J. Elwood and M. O. Eberhard, “Effective Stiffness of Reinforced Concrete Columns,” *SJ*, vol. 106, no. 4, pp. 476–484, Jul. 2009, doi: 10.14359/56613.
- [18] R. P. Dhakal and K. Maekawa, “Modeling for Postyield Buckling of Reinforcement,” *Journal of Structural Engineering*, vol. 128, no. 9, pp. 1139–1147, Sep. 2002, doi: 10.1061/(ASCE)0733-9445(2002)128:9(1139).
- [19] J. B. Mander, M. J. N. Priestley, and R. Park, “Theoretical Stress-Strain Model for Confined Concrete,” *Journal of Structural Engineering*, vol. 114, no. 8, pp. 1804–1826, Aug. 1988, doi: 10.1061/(ASCE)0733-9445(1988)114:8(1804).

Chapter 3

Parametric Studies on Seismic Response of Reinforced Concrete Arch Segments

Authors: Diego De la Mora and Jack P. Moehle

3.1 Abstract

This chapter investigates the seismic behavior of reinforced concrete arch ribs through a comprehensive parametric study using finite-element modeling in OpenSees. The study focuses on evaluating the influence of transverse reinforcement configuration and axial load ratio on the seismic performance of arch ribs to meet stringent seismic design criteria in California. Experimental data from scaled arch specimens representing typical bridge configurations were utilized to calibrate displacement-based fiber beam-column models in OpenSees. The analytical models were able to accurately replicate experimental findings, including displacement ductility and moment capacity under cyclic lateral displacements. The parametric study, validated against experimental results, demonstrates that increasing transverse reinforcement enhances deformation capacity. Additionally, increasing the axial force ratio reduces the drift ratio capacity of the section, while closer spacing of transverse reinforcement improves drift ratio capacities. All experimental specimens and analytical models achieved ductility capacities exceeding the requirements for seismic design in California.

3.2 Introduction

The California Department of Transportation (Caltrans) classifies bridges into three categories: Ordinary, Recovery, and Important. Within the Ordinary category, bridges are further delineated into "Standard" and "Non-Standard" based on various factors such as length, geometry, structural configuration, and geotechnical properties. Arch bridges typically experience significantly higher axial loads compared to conventional bridge columns, necessitating adherence to specific ductility requirements in accordance with the Caltrans Seismic Design Criteria (SDC) [1]. Arch bridges are occasionally classified as Ordinary Non-Standard. However, there are currently no provisions in place for Ordinary Standard Arch Bridges. Similarly to Caltrans, AASHTO does not provide any special consideration for the arch ribs' confinement reinforcement, indicating that these elements should be reinforced as compression members. This lack of guidelines caused bridges such as the Shasta Viaduct to have their initial design modified prior to construction, increasing the amount of transverse confinement reinforcement in the arch ribs.

An experimental program was conducted to investigate the influence of three primary parameters on the seismic response of reinforced concrete arches: confinement configuration, axial load ratio, and amount of transverse reinforcement. To conduct the experiment, two existing arch bridges in California were used as prototypes, the Spanish Creek Replacement and the Shasta Viaduct Replacement. These bridges are representative of two alternative confinement methods. Nine one-third scale test specimens were built following one of the two prototypes and tested under constant

axial compression and cyclic lateral displacements with increasing amplitudes. Each specimen was carefully designed to test the effects on the seismic performance of one of the three parameters of interest. The details of the experimental program and results for each test, such as displacement ductility and moment capacity, can be found in Chapter 2.

In this paper, the authors will present the development, calibration, and validation of the finite-element model of an arch rib section. The arch rib model was developed using the displacement-based fiber beam-column element from OpenSees [2]. The model is intended to replicate the specimens tested in the experimental program; therefore, the curvature of the arches was not replicated either in the experimental specimen or in the analytical model. The fiber material models of steel and concrete were calibrated using the material test data measured in the laboratory. The analytical model was calibrated using the experimental data obtained in the experimental program. The validated analytical models are used to perform a parametric study, allowing to obtain new data points by thus having a more robust dataset that complements the experimental measured data.

3.3 Research Significance

An analytical parametric study will provide a more robust set of data points to reliably establish the transverse reinforcement detailing requirements to ensure the ductile behavior of reinforced concrete arch ribs under axial loads greater than $0.15 A_g f'_c$. The parametric study performed in this paper looks to complement the experimental work presented in Chapter 2.

3.4 Literature Review

The SDC establishes a minimum transverse volumetric ratio, ρ_c , for Ordinary Standard Bridges in the plastic hinge region. These requirements are based on the element's aspect ratio, the confined section diameter, longitudinal reinforcement ratio, ρ_l , and axial load ratio. The specified minimum transverse volumetric ratio, $\rho_{c,min}$, ranges from 0.006 to 0.008 for Ordinary Standard Bridges. The volumetric confinement ratio, ρ_c , represents the volume ratio of transverse confinement reinforcement to the confined core, measured to the outside of the transverse reinforcement. For rectangular confined sections, it can be calculated using Equation (3.2) where $\sum A_{sx}$ and $\sum A_{sy}$ are the total areas of each hoop set parallel to b_c or h_c , s is the longitudinal spacing between hoop sets, and h_c or b_c is the confined core height or width measured to the outer perimeter of the hoop. These transverse reinforcement ratios can be expressed as ρ_{tx} and ρ_{ty} . For sections with a circular confined core, Equation (3.1) applies, where A_{sh} is the circular hoop bar area, s is the longitudinal spacing between hoops, and d_c is the diameter of the circular confined core measured to the outside of the hoops.

$$\rho_c = \rho_{tx} + \rho_{ty} = \frac{\sum A_{sx}}{s h_c} + \frac{\sum A_{sy}}{s b_c} \quad (3.2)$$

$$\rho_c = \frac{4A_{sh}}{s d_c} \quad (3.3)$$

However, these criteria account only for axial load ratios up to $0.15 A_g f'_c$, A_g is the gross cross-sectional area of the column, and f'_c is the concrete compressive strength. While previous researchers [3] have done test on columns under high axial load, the SDC considers that there are not enough data points to reliably establish a ductile behavior under axial loads greater than $0.15 A_g f'_c$.

For seismic members that do not conform to the parameters established by the SDC for Ordinary Standard Bridges, a minimum transverse volumetric ratio must be specified to ensure a ductility capacity of 3.0. In case a displacement capacity of 3.0 may be difficult to achieve, an acceptable $\rho_{c,min}$ may be established following a Project-Specific Design Criteria procedure.

Equation (3.4) can be used to compute the displacement capacity of an element, where μ_c is the displacement ductility capacity, Δ_c is the displacement capacity of the element and Δ_Y is the idealized yield displacement at the formation of the plastic hinge. The idealized yield displacement can be calculated for a cantilever column with Equation (3.5) where L is the column length, and ϕ_Y is the idealized yield curvature.

To determine the idealized yield curvature according to the SDC procedure, a moment-curvature analysis is performed and then idealized as an elastic-perfectly plastic response. The elastic portion of the idealized curve must pass through the point of first reinforcing bar yield. The idealized plastic moment capacity is achieved by balancing the areas between the actual and idealized moment-curvature curves beyond the initial yield point of the reinforcing bar. The idealized yield curvature, ϕ_Y , then, is the curvature at which the idealized elastic-perfectly plastic response becomes plastic.

$$\mu_c = \frac{\Delta_c}{\Delta_Y} \quad (3.4)$$

$$\Delta_Y^{col} = \frac{1}{3} L^2 \phi_Y \quad (3.5)$$

Elwood and Eberhard [4] propose an alternative method to determine the yield displacement, Δ_Y , of an element. First, perform a moment-curvature analysis to find the effective strength $M_{0.004}$, the theoretical moment when the extreme concrete fiber reaches a compressive strain of 0.004. A first yield point is defined as the moment at which the tension reinforcement yields or the maximum compressive concrete strain reaches 0.002, whichever comes first. A secant is then drawn from the origin through the first yield point on the moment-displacement backbone to its intersection with $M_{0.004}$. This intersection defines the effective yield displacement, Δ_Y . A similar procedure can be done to calculate the yield curvature, ϕ_Y , using the moment-curvature backbone instead.

Similarly to the SDC, AASHTO [5] does not contemplate special specifications for reinforced concrete arch ribs, requiring the same transverse reinforcement confinement specifications as any other element under compression. For a circular column, the minimum volumetric confinement ratio should satisfy Equation (3.6) where A_{sp} is the cross-sectional area of the reinforcement hoop,

d_c is the core diameter of the column measured to the outside diameter of the hoop, s is the spacing of hoops, f'_c is the compressive strength of concrete used in design and f_{yh} is the yield strength of the transverse reinforcement.

$$\rho_s = \frac{4A_{sp}}{(d_c s)} \geq 0.12 \frac{f'_c}{f_{yh}} \quad (3.6)$$

For rectangular columns, the total cross-sectional area of tie reinforcement, A_{sh} , should satisfy both Equation (3.7) and Equation (3.8) in regions where plastic hinges are expected. In this equations, new terms are introduced, A_g is the gross area of the section, A_c is the area of the column core measured to the outside of the reinforcement, and h_c is the confined core height or width measured to the outer perimeter of the hoop.

$$A_{sh} \geq 0.30 s h_c \frac{f'_c}{f_{yh}} \left[\frac{A_g}{A_c} - 1 \right] \quad (3.7)$$

$$A_{sh} \geq 0.12 s h_c \frac{f'_c}{f_{yh}} \quad (3.8)$$

The bridge prototypes selected for Chapter 2 were designed and constructed by Caltrans in California. The Spanish Creek Replacement Bridge arches were built with a rectangular cross section, utilizing rectilinear stirrups and crossies with alternating 90-degree and 135-degree hooks around the column perimeter. The Shasta Viaduct Replacement Bridge cross section consisted of a square cross-section with a circular core confined by circular hoops. The main longitudinal reinforcement is arranged in a circular pattern, with secondary longitudinal and transverse reinforcement placed outside the confined core. Both the Spanish Creek Replacement Bridge and the Shasta Viaduct Replacement are bridges in California that Caltrans classifies as Ordinary Standard Bridges. The Spanish Creek Replacement Bridge arch has a rectangular section of 106 x 94.5 in., with a longitudinal reinforcement ratio, ρ_l , of 0.014, a volumetric confinement ratio of 0.014, and a s/d_b equal to 2.4, where s is the transverse reinforcement spacing and d_b is the longitudinal bar diameter. The Shasta Viaduct Replacement prototype had a square cross section of 84 in., a longitudinal reinforcement ratio of 0.010, an original volumetric confinement ratio of 0.007 that was later increased to 0.013 by doubling the number of hoops, and an s/d_b ratio of 3.5.

3.5 Finite Element-Model

Miller [6] studied and modeled Specimen 4 in Chapter 2. In this work, Miller used OpenSees to calibrate and validate an analytical model of Specimen 4. In this analytical model, a column of the same length as the experimental column ($L = 162$ in.) was modeled with a fixed base. The column was subdivided into five elements (Figure 3.1) resulting in elements with an approximate length of one section depth. The column elements were modeled using *displacement-based beam-column elements* that allow the spread of plasticity through the fiber sections.

Expanding Miller’s work, a cantilever column model or specimens 3 to 9 in Chapter 2 was created using OpenSees. Each model consisted of a straight fixed-base column with a length equal to the test specimen $L = 4.11 \text{ m}$ (162 in.). Each one of the arch ribs was modeled in OpenSees using *displacement-based beam-column elements*. The column was divided into five elements, resulting in element lengths slightly greater than one section depth. Each beam-column element used two Gauss-Legendre integration points. Fiber cross sections were assigned to the integration points. The cross sections of the elements were taken from the experimental tests. These cross sections consisted of steel and concrete fibers.

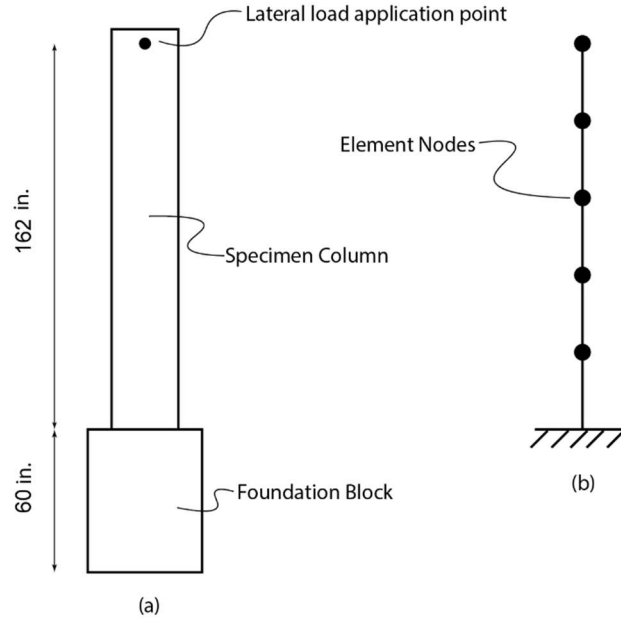


Figure 3.1. (a) Experimental arch rib Specimen dimensions. (b) Discrete structural model.

A *displacement-based beam-column element* uses deformation shape functions to relate nodal element displacements to element deformations. Constitutive material relationships are used to determine stresses in the element. Said stresses are integrated at each integration point to determine the section and element stiffness matrix and, finally, obtain the resisting forces. [7]. By refining the mesh (reducing the element size), the accuracy of these elements can be improved. Displacement-based elements assume a constant axial deformation and a linear curvature distribution along the element length, therefore increasing the number integration points does not produce a more accurate result.

An alternative to the *displacement-based beam-column element* in OpenSees, is the *force-based beam-column element*. The force-based elements can be modeled by a single element, and the accuracy of the solution can be improved by increasing the number of integration points. However, both formulations present problems when the element response starts to present softening. In the displacement-based element case, the length of the element undergoing softening controls the structural response and can lead to inaccurate deformation concentrations if the mesh size is too small. On the other hand, in a force-based element, the deformations are localized at a single integration point, which can also lead to large deformation concentrations. Some researchers have

proposed different methods, [8] and [9], to address the softening in force-based elements, but for a displacement-based element the best solution is to not over-refine the element mesh size.

Each material in the cross section is defined with a uniaxial stress-strain relationship that was calibrated with the measured material properties used in each specimen. Every fiber section in the model was divided into either concrete cover, concrete core, primary reinforcing steel, secondary reinforcing steel (when applicable), and steel pipe (when applicable).

OpenSees offers several uniaxial materials to model concrete. For this study, *Concrete04* was selected and assigned to concrete cover and concrete core fibers. *Concrete04* model utilizes the Popovics stress-strain curve [10] which was utilized to develop the Mander *et al.* [11] stress-strain model for confined concrete. The concrete cover (unconfined concrete) parameters were taken from the companion cylinder compression tests. The confinement reinforcement was not modeled in the fiber section, but the confinement effects were applied to the concrete core fibers following the model proposed by Mander. The strain at peak confined stress, ε_{cc} , was calculated using the Equation (3.9) proposed by Richart *et al.* [12].

$$\varepsilon_{cc} = \varepsilon_c \left[1 + 5 \left(\frac{f'_{cc}}{f'_c} - 1 \right) \right] \quad (3.9)$$

The ultimate confined concrete strain, ε_{ccu} , was calculated using Equation (3.10) by Priestley *et al.* [13]. As noted by the authors, this equation was specifically formulated for elements under compression, which may result in conservative estimates for sections subjected to both bending and axial compression. For this reason, the value ε_{cu} for each specimen was scaled to better reflect the experimental behavior observed. Alternative expressions for determining the ultimate strain capacity for confined concrete, such as those proposed by Scott *et al.* [14] and Moehle [15], have similarly conservative expressions, particularly for circular hoop-confined columns. Typical stress-strain curve relationships for the unconfined concrete cover and confined concrete core modeled with *Concrete04* are shown in Figure 3.2a.

$$\varepsilon_{ccu} = 0.004 + \frac{1.4\rho_s f_{yh} \varepsilon_{su}}{f'_{cc}} \quad (3.10)$$

Steel fibers were modeled using the OpenSees uniaxial *ReinforcingSteel* material [16], this material model uses a nonlinear backbone curve. The tensile properties for the longitudinal reinforcement were taken from measured values reported in Chapter 2. The *ReinforcingSteel* material uses the buckling model based on Gomes and Appleton [17]. Figure 3.2b illustrates the stress-strain relationship for the different types of steel fibers, primary longitudinal bars and secondary longitudinal reinforcement bars.

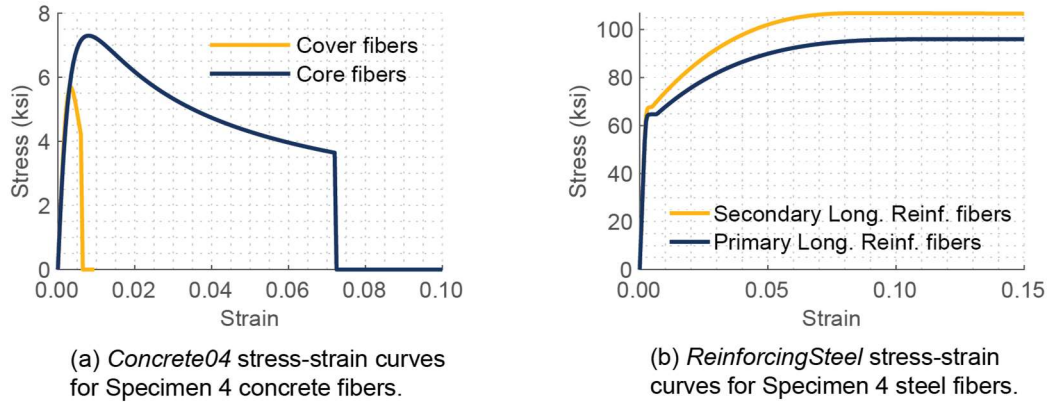


Figure 3.2. Typical strain-stress relationship for the materials utilized in analytical models.

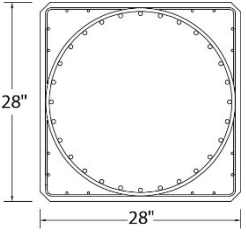
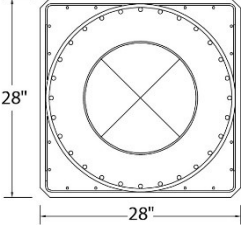
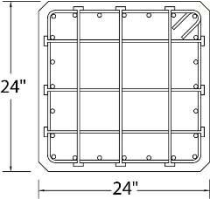
Anchorage slip at joints or foundation interfaces can contribute significantly to the overall member deformation capacity, for example, Lehman and Moehle [18] showed that the anchorage slip component can be even greater than the flexural displacement component in some cases. However, Elwood and Eberhard [4] found that for columns under high axial load, the slip contribution to total displacement decreases. Miller studied analytical modeling of anchorage slip effects for Specimen 4, employing rotational springs and *Zero-Length fiber elements* at the column base, concluding that current methods for modeling bar slip are inadequate for softening sections and that a nonlinear beam-element can adequately approximate the member behavior.

3.6 Calibration and Model Validation

Specimens 1 and 2 rectangular cores were confined with rectilinear stirrups and crossties, and tested under axial force ratios $P/A_g f'_c$ of 0.25 and 0.40, respectively. These two specimens followed the Spanish Creek Replacement Bridge prototype transverse reinforcement configuration. Specimens 3 to 6 had rectangular cross sections with circular confined cores, achieved using butt-welded circular hoops with primary longitudinal reinforcement placed in a circular array inside the circular hoops. Secondary No.3 longitudinal were placed outside the confined core inside U-shaped rectilinear hoops that were lap-spliced to create a continuous hoop. Axial force ratio, transverse reinforcement ratio, and spacing were varied. Specimen 7, with a similar configuration as Specimen 6, included a hollow section with a 406 mm (16 inches) diameter steel pipe (6 mm thick ASTM A500 Grade C) at the center, extending approximately 13 mm (1/2 inch) into the foundation block to resist core concrete dilation without significantly contributing to moment resistance. Specimens 8 and 9 had square confined cores with rectilinear perimeter hoops and double-headed crossties. The crossties had 32 mm (1.25 inch) square heads welded to 10 mm (No. 3) bars, providing a bearing area equal to 14 times the reinforcement bar area $14A_b$.

This parametric study focuses on Specimens 3 to 9. A summary of the experimental specimens is shown in Table 3.1. This table presents the specimen cross section, the companion cylinder compressive strength at 28 days, f'_c , the volumetric confinement ratio, ρ_c , the transverse reinforcement spacing, s , the longitudinal reinforcement diameter, d_b , the ratio s/d_b , the applied axial force, P , and the axial force ratio $P/A_g f'_c$. For more detailed information see Chapter 2.

Table 3.1. Properties and details of test specimens.

Specimen	Cross Section	f'_c , MPa [ksi]	ρ_c	s, mm [in]	s/db	P, kN [kips]	$P/A_g f'_c$
3		34.5 [5.01]	0.008	101.6 [4]	6.4	4340 [975]	0.25
4		39.4 [5.71]	0.015	50.8 [2]	3.2	4870 [1100]	0.25
5		33.0 [4.79]	0.015	50.8 [2]	3.2	6650 [1500]	0.40
6		29.9 [4.34]	0.008	50.8 [2]	3.2	3780 [850]	0.25
7		29.4 [4.26]	0.008	50.8 [2]	3.2	2450 [550]	0.16
8		33.1 [4.80]	0.024	50.8 [2]	3.2	3070 [690]	0.25
9		33.1 [4.80]	0.016	76.2 [3]	4.8	3070 [690]	0.25

The load protocol consisted of applying a constant axial compressive force maintained throughout the test. Lateral displacement was applied at the specimen tip, following FEMA 461 guidelines [19], with cyclic lateral displacements increasing progressively. Specimens 1 to 7 underwent two displacement cycles per step, while Specimens 8 and 9 had three cycles per step. Each displacement step amplitude was 1.4 times the previous step, except for Specimens 1 and 3, which used a factor of 1.5. The initial target displacement was selected to ensure that three to four steps were completed before reaching the effective yield point of the critical section.

The fiber cross section assigned to the *displacement-based beam-column elements* aimed to replicate the actual specimen cross-sections as accurately as possible. Figure 3.3 illustrates the three different cross sections used. Cross section S (Figure 3.3a) was utilized to model Specimen 3 to Specimen 6; the concrete cover, shown in a lighter grey shade, is composed of 84 fibers. Similarly, the concrete core is modeled with 84 fibers. Specimen 7 was modeled with Cross section P (Figure 3.3b), which included 117 fibers for the concrete cover and 86 fibers for the confined core. Cross section H (Figure 3.3c) was assigned to Specimens 8 and 9, utilizing 88 fibers for the concrete cover and 60 fibers for the concrete core. In all cases, the main and secondary longitudinal (when applicable) reinforcement was modeled with steel fibers.

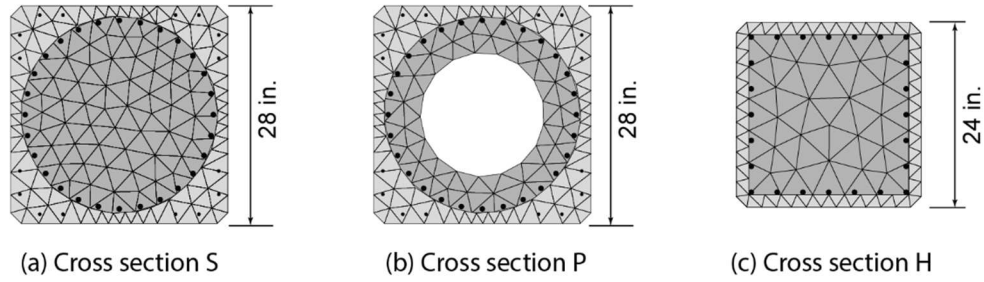


Figure 3.3. Fiber section meshes.

Table 3.2 shows the parameters used to define the *Concrete04* uniaxial material in OpenSees for models using cross section S. The crushing strain of the confined concrete is expressed in terms of the ultimate confined concrete strain, ϵ_{ccu} . Table 3.3 shows the material input parameters for the *ReinforcingSteel* uniaxial material. For simplicity, and due to the closeness of the measured values, longitudinal reinforcement was modeled with the same inputs for all the analytical models.

Table 3.2. Material input parameters for Beam-Column Element Fiber Sections Type S.

		Specimen 3	Specimen 4	Specimen 5	Specimen 6				
Geometry									
Cross Section Type				S					
Outer dimensions (in)				28x28					
Core diameter (in)				26.5					
Primary (No.5) bars				28					
Secondary (No.3) bars				16					
Concrete04 fibers									
		Cover	Core	Cover	Core	Cover	Core	Cover	Core
Peak stress (ksi)	f'_c	4.9	6.4	5.7	7.3	4.8	6.2	4.3	6.1
Strain at peak stress	ϵ_c	0.0033	0.008	0.0033	0.008	0.0033	0.009	0.0033	0.009
Crushing strain	ϵ_{cu}	0.006	$1.50\epsilon_{ccu}$	0.006	$3.00\epsilon_{ccu}$	0.006	$1.50\epsilon_{ccu}$	0.006	$1.85\epsilon_{ccu}$
Initial stiffness (ksi)	E_c	2550	2550	2780	2780	2900	2900	2810	2810

These columns were subjected to the same load protocol as their experimental counterparts. A constant axial load was applied and held constant, followed by the same lateral displacement protocol as the experimental model. Figure 3.4 comprises two rows of plots. The first row compares the experimental and analytical moment-drift ratio relationships. The drift ratio, δ , expressed as a percentage, represents the displacement at the tip of the cantilever column relative to the column length. The Y-axis represents the bending moment at the column base, assuming the axial force acts at the geometric centroid of the column cross section. The second row of plots compares the experimental and analytical moment-drift ratio backbones. The average backbone curves were determined, for both cases, according to ASCE 41-17 [20]. The Y-axis is in terms of the normalized moment, which is the moment divided by the maximum moment of each corresponding backbone, M_{max} . The ultimate displacement, Δ_{80} , is defined as displacement when the moment capacity of the element decays to 80% of the maximum moment for the analytical model. The ultimate displacement is marked in Figure 3.4 with a yellow triangle.

In these figures the initial stiffness and yield displacement are adequately modeled, however, as the sections start to present damage, there are some discrepancies in moment capacity especially due to spalling (see Figure 3.4f). The analytical model was stopped at the peak displacement imposed during the test.

Table 3.3. *ReinforcingSteel* input parameters for analytical models.

ReinforcingSteel fibers		Primary	Secondary
Yield stress (ksi)	f_y	64.7	67.7
Ultimate stress (ksi)	f_u	96	106.8
Elastic modulus (ksi)	E_s	27400	27945
Initial hardening stiffness	E_{sh}	$0.35E_s$	$0.45E_s$
Strain at onset of hardening	ϵ_{sh}	0.0066	0.0048
Strain at ultimate stress	ϵ_u	0.12	0.084
Buckling Model	GA	Gomes and Appleton Buckling Model [17]	
GA buckling parameters			
Slenderness ratio	l_{sr}	s/d_b^a	10.7
Curve amplification factor	β	2.0	2.0
Reduction factor	r	0	0
Buckling constant	γ	0.5	0.5

^aThe slenderness ratio value used for each model is the s/d_b ratio shown in Table 3.1.

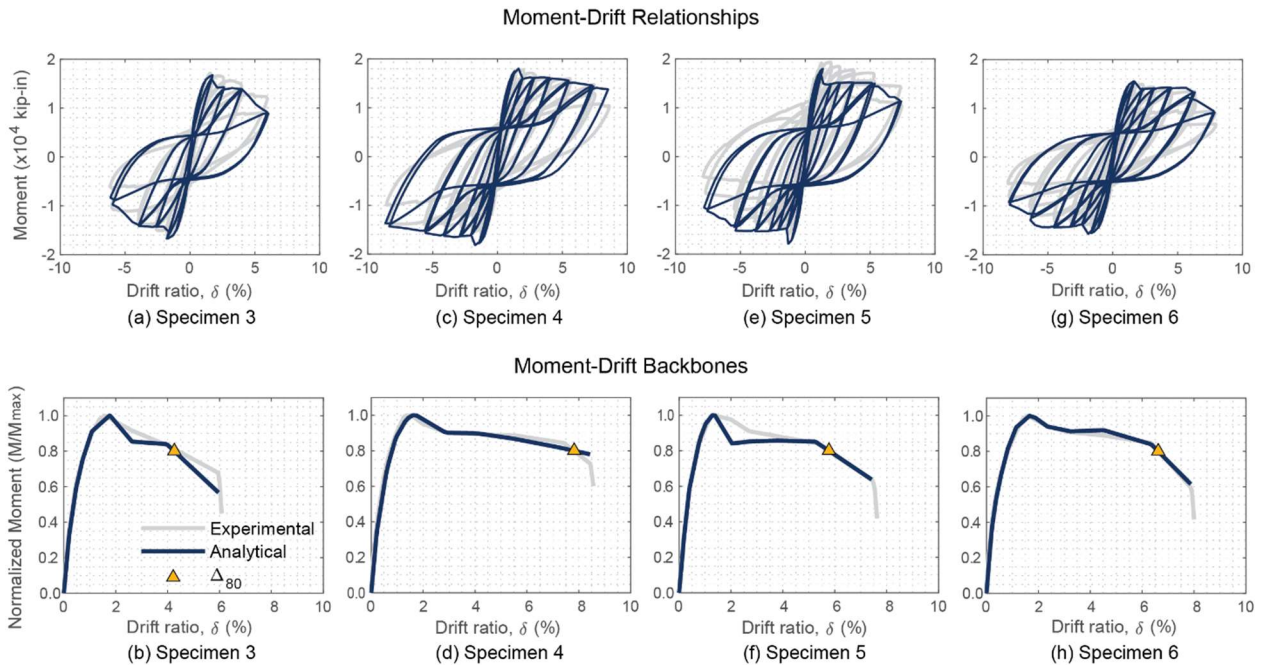


Figure 3.4. Moment-drift ratio relationships, and Moment-drift ratio backbones for Sections Type S.

Table 3.2 presented values for the ultimate concrete crushing strain of the confined core in terms of ϵ_{ccu} obtained from Equation (3.10). This is because current expressions for modeling ultimate confined concrete strain capacity tend to underestimate strain capacity. Figure 3.5 compare two models for Specimen 4. Figure 3.5a is the moment-drift and moment-curvature relationship for Specimen 4 using as input for the ultimate confined concrete strain the value obtained using Equation (3.10), while Figure 3.5b shows the same relationships for a model with the ultimate confined concrete strain adjusted to match the experimental behavior. Figure 3.5a present an early and sudden drop in moment capacity that does not adequately represent the behavior measured in the experimental tests. This behavior was true for all models with a circular confined core; therefore, ϵ_{ccu} was adjusted using an empirical scale factor in all specimens to better recreate the experimental data.

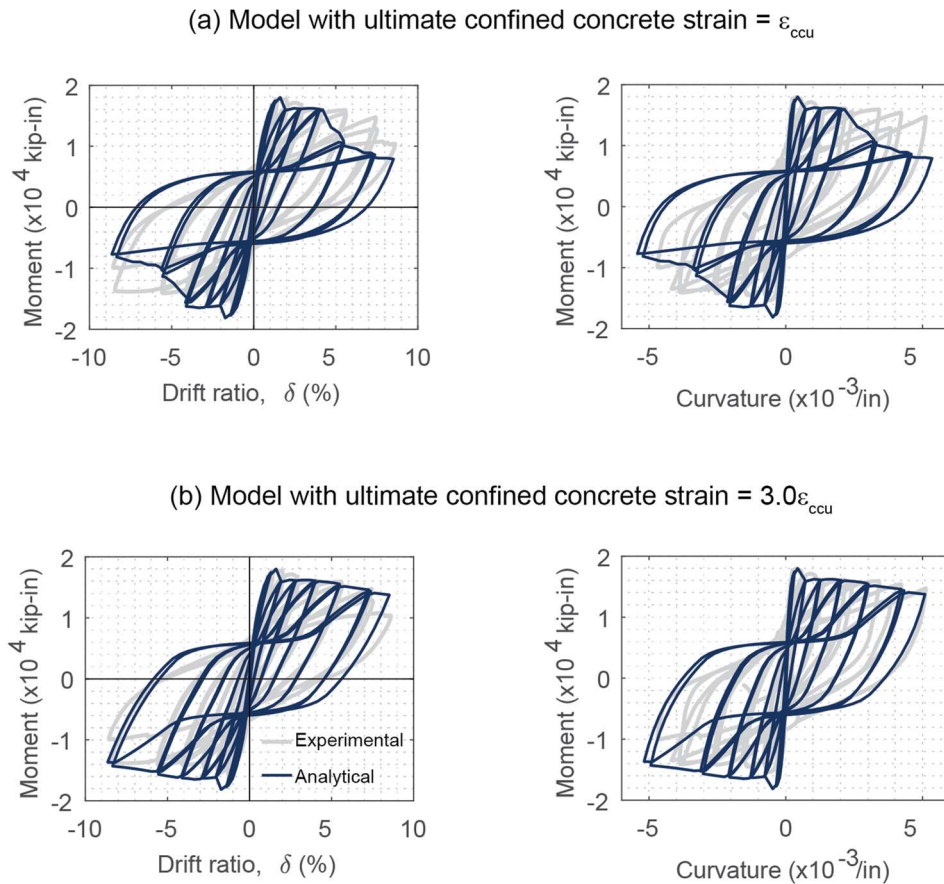


Figure 3.5. Moment-drift and moment-curvature comparison for Specimen 4 model with different ultimate confined concrete strain input.

Specimen 7 had a hollow cross section with a steel pipe placed at the center of the cross section with the intention to resist core concrete dilation without significantly contributing to moment resistance. The steel pipe was intentionally not embedded into the foundation block to minimize

its contribution to the resisting bending moment. To replicate this non-contribution, the steel fibers corresponding to the steel pipe section were not modeled. Table 3.4 presents the parametric inputs that were used to define the uniaxial materials that form the fibers for Specimen 7. Reinforcing steel properties are shown in Table 3.3. Similarly, to the previous specimens, Figure 3.6 presents the moment-drift relationship and moment-drift backbone for Specimen 7. The numerical model adequately mimics the initial stiffness behavior. However, the experimental test presents a yield plateau that is not present in the analytical model. The descending branch in the experimental model is more pronounced than the analytical model, suggesting a more brittle behavior than the one modeled.

Table 3.4. Material input parameters for Beam-Column Element Fiber Section Type P.

Specimen 7			
Geometry			
Cross Section Type		P	
Outer dimensions (in)		28x28	
Core diameter (in)		26.5	
Inner hole diameter (in)		16	
Primary (No.5) bars		28	
Secondary (No.3) bars		16	
Concrete04 fibers		Cover	Core
Peak stress (ksi)	f'_c	4.3	6.0
Strain at peak stress	ϵ_c	0.0033	0.010
Crushing strain	ϵ_{cu}	0.006	$1.75\epsilon_{ccu}$
Initial stiffness (ksi)	E_c	2960	2960

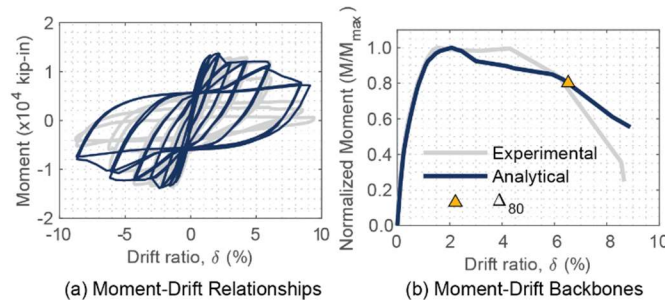


Figure 3.6. Moment-drift ratio relationships, and Moment-drift ratio backbones for Sections Type P.

Specimens 8 and 9 had square confined cores with rectilinear hoops in the perimeter and double-headed cross-ties. Cross section H (Figure 3.3c) was used to model the cross section for these specimens. Table 3.5 presents the fiber model details and input parameters for *Concrete04* uniaxial material in OpenSees. The material input parameters for the longitudinal reinforcement are also provided in Table 3.5. Figure 3.7 shows the experimental and analytical moment-drift relationships for Specimens 8 and 9, as well as a comparison of the moment-drift backbones. Figure 3.7 shows

that the analytical models for Specimens 8 and 9 adequately represent the behavior of the sections. The initial stiffness, yield displacement, and descending branch are consistent with the experimental data. Specimen 8 did not exhibit a 20% loss of capacity by the end of the test; therefore, in this case, Δ_{80} was defined as the maximum displacement achieved by the section during testing.

Table 3.5. Material input parameters for Beam-Column Element Fiber Sections Type H.

		Specimen 8		Specimen 9	
Geometry					
Cross Section Type		H			
Outer dimensions (in)		24x24			
Primary (No.5) bars		28			
Concrete04 fibers		Cover	Core	Cover	Core
Peak stress (ksi)	f'_c	4.8	8.5	4.8	7.5
Strain at peak stress	ϵ_c	0.0033	0.0015	0.0033	0.008
Crushing strain	ϵ_{cu}	0.006	$0.83\epsilon_{ccu}$	0.006	$0.86\epsilon_{ccu}$
Initial stiffness (ksi)	E_c	3050	3050	2780	2780

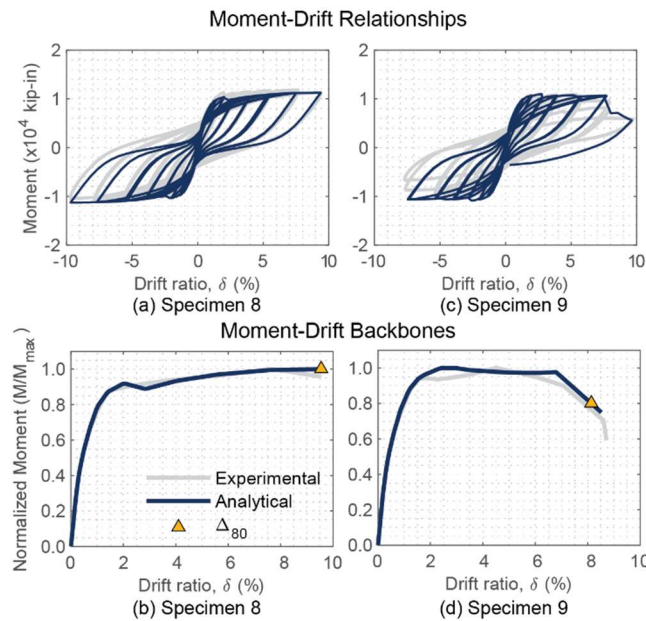


Figure 3.7. Moment-drift ratio relationships, and Moment-drift ratio backbones for Sections Type H.

Opposite to the specimens with circular confined core, the specimens with a rectangular cross section and rectangular confinement needed to reduce the ultimate confined concrete strain

obtained using Equation (3.10). Figure 3.8 compares the results obtained using Specimen 9 model with an unscaled ε_{ccu} and a model with an adjusted ε_{ccu} . The model with an adjusted ε_{ccu} represents more adequately the behavior obtained from the experimental tests. The reduced strain capacity in the confined concrete produces a drop in moment capacity at large drifts, which matches the observed experimental behavior.

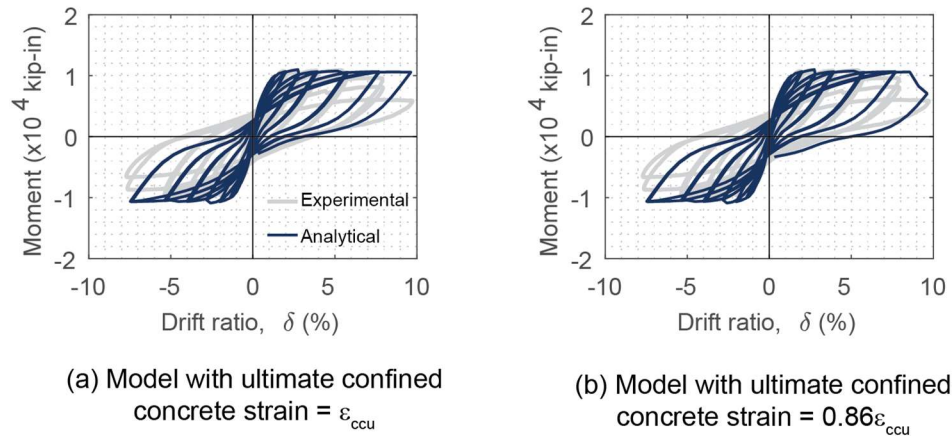


Figure 3.8. Moment-drift comparison for Specimen 9 model with different ultimate confined concrete strain input.

Table 3.6 presents M_{max} values for the experimental test results and the analytical backbones. The ultimate drift ratio for both cases is also shown. The ultimate drift ratio for the analytical model corresponds to a loss of 20% capacity of the maximum analytical backbone moment. The analytical model error was calculated by subtracting the analytical value from the experimental value and then dividing the result by the experimental value. Table 3.6 presents the M_{max} error and Drift Ratio (%) at Δ_{80} error in percentage.

The maximum moment capacity is adequately modeled in the numerical analysis, overestimating the experimental moment capacity with less than 10% error in all cases. The ultimate drift capacity is also well modeled, with less than 5% error for all specimens. Specimen 8, which presented less damage during the test, has the analytical model that better represents the behavior, suggesting that the modeled damaged behavior of the section can still be refined.

Table 3.6. Experimental and analytical calibration results summary.

Specimen	$M_{max}, \text{kN}\cdot\text{m} \times 10^3$ [kip-ft $\times 10^3$]			Drift Ratio (%) at Δ_{80}		
	Experimental	Analytical	Error (%)	Experimental	Analytical	Error (%)
3	1.87 [1.38]	1.88 [1.39]	0.9%	4.41	4.26	-3.4%
4	1.91 [1.41]	2.03 [1.50]	6.3%	7.81	7.82	0.2%
5	1.97 [1.45]	2.00 [1.48]	2.2%	5.76	5.78	0.3%
6	1.66 [1.22]	1.76 [1.30]	6.3%	6.64	6.62	-0.3%
7	1.44 [1.06]	1.54 [1.14]	7.3%	6.35	6.52	2.7%
8	1.27 [0.94]	1.27 [0.94]	-0.1%	9.54	9.55	0.1%
9	1.19 [0.88]	1.23 [0.91]	2.8%	7.86	8.14	3.5%

For completion, the moment-curvature comparison of the analytical model with the experimental model is shown for two cross section representative specimens. Figure 3.9a shows the moment-curvature at the column-base joint for Specimen 4. The numerical analysis adequately models the moment-curvature even at large curvatures. Models of specimens with a square cross section and circular confined core presented similar behavior to the one shown in this figure. Figure 3.9b shows the moment-curvature at the column-base joint for Specimen 8. For specimens with a square cross section and headed bars, the numerical model underestimates the curvature at large displacements compared with the experimental data.

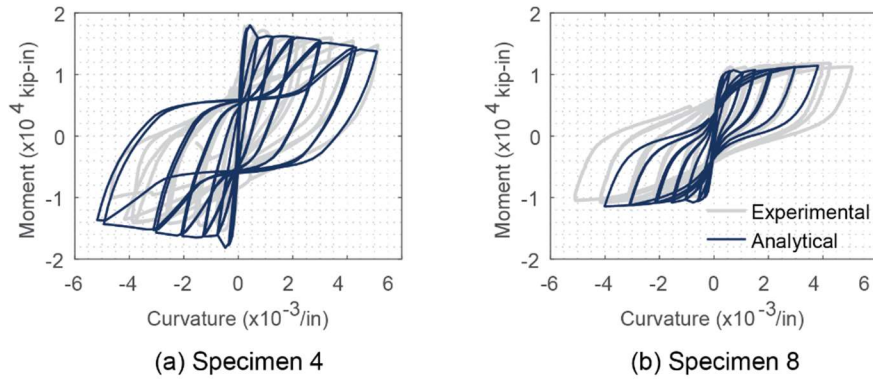


Figure 3.9. Experimental and Analytical moment-curvature relationships.

3.7 Parametric Studies

The parametric study involved varying key parameters to assess their impact on structural response. Parameters such as axial load, volumetric confinement ratio, and longitudinal bar buckling restraining ratio, s/d_b , were systematically varied across eight analytical models. Additionally, one model incorporated extra displacement amplitudes to overcome the physical test limitations and achieve an ultimate displacement, Δ_{80} , in Specimen 8. The analytical models were sequentially numbered following the experimental tests. Table 3.7 presents the key parameters for all analytical models, including the experimental test base model, cross-section type, displacement protocol utilized, volumetric confinement ratio, transverse reinforcement bar size, transverse reinforcement spacing, s , s/d_b ratio, using 16 mm (No. 5) bars as longitudinal reinforcement, axial load, P , and axial force ratio $P/A_g f'_c$.

To create these analytical models, a characteristic experimental test model was used as the base. The base experimental model was selected to minimize the variables modified to investigate the parameter of interest and to preserve as possible the integrity of the simulation. Therefore, these models adopted the same cross-section type and load protocol as the base model. The material properties in the models were also consistent with the base model.

The first three analytical models, Models 10 to 12, were based on test specimens with cross-section type S, consisting of a square section with a circular confined core achieved with circular hoops. Model 10 was modeled after Specimen 6 and tested under high axial load ($0.40 A_g f'_c$). Models 11 and 12 were based on Specimen 4, with the transverse reinforcement spacing increased to 7.6 mm (3 in.), modifying the confined concrete parameters and s/d_b ratio. Models 11 and 12 were subjected to moderate and high axial loads, respectively.

Model 13 to 14 explored the behavior of a hollow cross section reinforced with a steel pipe. Specimen 7 served as a base model. Model 13 maintained the same reinforcement configuration as the base model and was tested under a high axial load ($0.25 A_g f'_c$). Model 14, the original volumetric confinement ratio was increased by using 11 mm (No. 4) bars as transverse reinforcement while keeping the same spacing, with confined concrete values adjusted according to Mander *et al.* [11] stress-strain model.

The last four models in this study utilized cross-section type H. Model 15 was based on Specimen 8 and tested under high axial load. Similarly, Model 16 followed Specimen 9 configuration and was tested with a high axial load ratio. Model 17 also used Specimen 9 as the base but increased the transverse reinforcement bar size from 9.5 mm (No. 3) bars to 11 mm (No. 4) bars, thereby increasing the volumetric confinement ratio. Model 18 replicates the test configuration and loading protocol of Specimen 8. However, an additional incremental displacement amplitude step with two cycles was applied to the original displacement protocol to obtain a theoretical Δ_{80} for this section.

Table 3.7. Principal parameters in analytical models.

Model	Experimental Specimen Base	Cross Section Type	Displacement Protocol	ρ_c	s, (mm) [in]	s/d _b	P, (kN) [kips]	P/A _g f' _c
10	Specimen 6	S	Specimen 6	0.008	50 [2]	3.2	6050 [1360]	0.40
11	Specimen 4	S	Specimen 4	0.010	76 [3]	4.8	4980 [1120]	0.25
12	Specimen 4	S	Specimen 4	0.010	76 [3]	4.8	7960 [1790]	0.40
13	Specimen 7	P	Specimen 7	0.008	50 [2]	3.2	3715 [835]	0.25
14	Specimen 7	P	Specimen 7	0.015	50 [2]	3.2	2450 [550]	0.16
15	Specimen 8	H	Specimen 8	0.024	50 [2]	3.2	4915 [1105]	0.40
16	Specimen 9	H	Specimen 9	0.016	76 [3]	4.8	4915 [1105]	0.40
17	Specimen 9	H	Specimen 9	0.030	76 [3]	4.8	3070 [690]	0.25
18	Specimen 8	H	Extended Specimen 8	0.016	50 [2]	3.2	3070 [690]	0.25

As shown in the previous section, the current expressions for modeling ultimate confined concrete strain capacity tend to underestimate strain capacity. Determining an accurate ϵ_{ccu} is crucial for obtaining a precise model behavior. To reflect the actual measured experimental behavior, it was necessary to scale the ultimate confined concrete strain computed using Equation (3.10). Columns with circular hoop confinement required scaling up, sometimes by factors of up to three times the calculated value when no damage was present in the transverse reinforcement. Conversely, columns with rectilinear transverse reinforcement required scaling down the ultimate confined strain capacity, regardless of the damage level in the transverse reinforcement at the end of testing. High axial loads increased section damage, reducing the displacement ductility capacity of the section presented in Chapter 2, yet the theoretical ultimate confined concrete strain still needed to be scaled up to match experimental behavior.

Table 3.8 presents the theoretical strain values for ϵ_{ccu} using Equation (3.10), the strain values used in the model, and the corresponding applied scale factor. The table is divided into two main sections. For the first section, corresponding to the validated models, scale factors were assigned empirically to represent experimental behavior. For the second section, the scale factor was chosen based on validated models with similar characteristics (geometry, axial force ratio, or volumetric confinement ratio) to each parametric model.

Columns with circular hoops used as confinement reinforcement expected to exhibit high damage at the end of testing (due to poor confinement or high axial load) were appropriately scaled by a factor of 1.50 to reflect the strain values necessary to model substantial deterioration in the confined core. For cases where moderate damage was anticipated in the confined core or transverse

reinforcement, scale factors of 1.75 to 1.85 ϵ_{ccu} provided a suitable fit. Well-confined models without transverse reinforcement fracture were modeled using three times the estimated ultimate strain capacity. In contrast, the ultimate confined concrete capacity for sections with rectilinear reinforcement had to be scaled down with a scale factor of 0.85.

Using the theoretical ϵ_{ccu} value seemed overly conservative, potentially producing smaller ultimate displacement capacities Δ_{80} and displacement ductility. Therefore, it was deemed inappropriate to use Equation (3.10) without a scale factor for the parametric models. The second section in Table 3.8 shows the theoretical, used, and scale factors employed in the parametric models. These values were selected based on observations from the calibration models.

Table 3.8. Ultimate confined concrete strain capacity.

	Theoretical ϵ_{ccu}^a	ϵ_{ccu} utilized in model	Scale Factor
Specimen 3	0.018	0.027	1.50
Specimen 4	0.024	0.072	3.00
Specimen 5	0.027	0.040	1.50
Specimen 6	0.020	0.037	1.85
Specimen 7	0.020	0.035	1.75
Specimen 8	0.036	0.030	0.83
Specimen 9	0.029	0.025	0.86
Model 10	0.019	0.030	1.50
Model 11	0.019	0.035	1.85
Model 12	0.019	0.029	1.50
Model 13	0.020	0.031	1.50
Model 14	0.028	0.049	1.75
Model 15	0.036	0.031	0.85
Model 16	0.029	0.025	0.85
Model 17	0.048	0.041	0.85
Model 18	0.036	0.031	0.85

^a ϵ_{ccu} obtained using Equation (3.9)

Table 3.9 presents the input parameters utilized to model the concrete fibers in the analytical parametric models, using *Concrete04* as material in OpenSees. Confined concrete core fiber inputs were calculated using the parametric transverse confinement reinforcement configuration. Reinforcing steel was modeled using the *ReinforcingSteel* material, with its input parameters outlined in Table 3.3.

Table 3.9. *Concrete04* input parameters for parametric models.

	Unconfined Cover Concrete fibers				Confined Core Concrete fibers			
	Peak Stress (ksi)	Strain at peak stress	Crushing strain	Initial stiffness (ksi)	Peak Stress (ksi)	Strain at peak stress	Crushing strain	Initial stiffness (ksi)
	f'_c	ϵ_c	ϵ_{cu}	E_c	f'_c	ϵ_c	ϵ_{cu}	E_c
Model 10	4.3	0.0033	0.006	2810	6.1	0.0100	$1.50\epsilon_{ccu}$	2810
Model 11	5.7	0.0033	0.006	2870	7.3	0.0120	$1.85\epsilon_{ccu}$	2870
Model 12	5.7	0.0033	0.006	2870	7.3	0.0120	$1.50\epsilon_{ccu}$	2870
Model 13	4.3	0.0033	0.006	2960	6.0	0.0100	$1.75\epsilon_{ccu}$	2780
Model 14	4.3	0.0033	0.006	2960	7.1	0.0140	$1.50\epsilon_{ccu}$	2780
Model 15	4.8	0.0033	0.006	3050	8.5	0.0150	$0.85\epsilon_{ccu}$	3050
Model 16	4.8	0.0033	0.006	3070	7.5	0.0080	$0.85\epsilon_{ccu}$	3070
Model 17	4.8	0.0033	0.006	3070	9.0	0.0080	$0.85\epsilon_{ccu}$	3070
Model 18	4.8	0.0033	0.006	3050	8.5	0.0150	$0.85\epsilon_{ccu}$	3050

Figure 3.10 displays the relationship between the normalized moment at the column base and the lateral drift ratio, along with the average backbone curves. Moment-drift ratio backbone curves were determined according to ASCE 41-17 for both loading directions. For a given drift ratio, the absolute moments from loading in opposite directions were averaged and normalized by the maximum average moment, M_{max} . The primary X-axis indicates the drift ratio (in percentage), while the secondary X-axis at the top shows the specimen displacement ductility, Δ_y/Δ_{80} . The primary Y-axis represents the normalized bending moment at the column base and the secondary Y-axis indicates the bending moment magnitude in kip-ft.

The procedure described by Elwood and Eberhard was utilized to determine an effective yield displacement Δ_y . To obtain Δ_y , a moment-curvature analysis was done for each model, utilizing the measured steel properties of the experimental base model. The post-yield buckling behavior was adjusted following the method proposed by Dhakal *et al.* [21]. The stress-strain relationships for the confined core concrete and unconfined cover concrete were modeled according to Mander *et al.* [11]. The analysis assumed that plane sections remain plane.

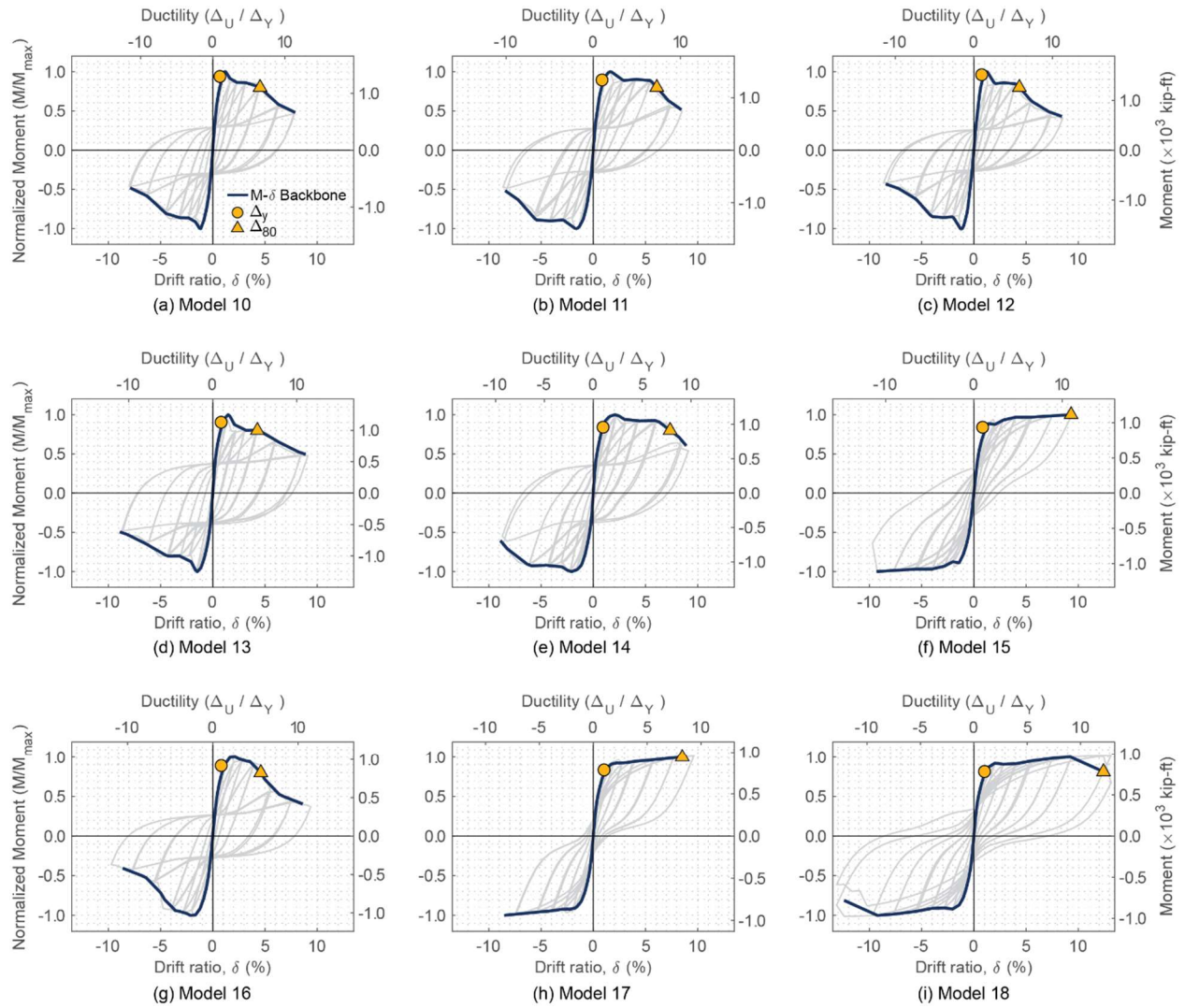


Figure 3.10. Parametric models Moment-Drift relationship.

Table 3.10 summarizes the performance metrics for the parametric models, such as the maximum average moment M_{max} , drift ratios at yield displacement Δ_y , and drift ratio at ultimate displacement Δ_{80} , and displacement ductility. Models 15 and 17 did not presented a 20% loss of capacity, therefore the largest drift ratio achieved was utilized as ultimate displacement.

Table 3.10. Parametric models results summary.

Model	M_{max} , kN-m x10 ³ [kip-ft x10 ³]	Drift Ratio (%) at Δ_y	Drift Ratio (%) at Δ_{80}	Displacement Ductility, Δ_{80}/Δ_y
10	1.87 [1.38]	0.69	4.53	6.58
11	2.02 [1.49]	0.83	6.08	7.29
12	2.13 [1.57]	0.75	4.35	5.80
13	1.69 [1.25]	0.80	4.27	5.32
14	1.55 [1.14]	0.93	7.35	7.86
15	1.51 [1.11]	0.84	9.31 ^a	11.02
16	1.40 [1.03]	0.81	4.60	5.65
17	1.27 [0.94]	1.03	8.52 ^a	8.25
18	1.31 [0.96]	1.02	12.41	12.14

^a Model did not reach Δ_{80} , the last displacement cycle is reported instead.

3.8 Discussion

Using specialized software like OpenSees is appropriate for modeling the behavior of experimental reinforced concrete columns and arch ribs. The fiber cross-section displacement-based beam-column elements with distributed plasticity effectively capture this behavior. Reinforcing steel fibers modeled with the *ReinforcingSteel* material in OpenSees accurately replicate the longitudinal reinforcing steel used in the experimental test specimens. *Concrete04* in OpenSees can model both confined and unconfined concrete fibers accurately. However, determining an appropriate ultimate strain capacity for confined concrete is crucial. Current expressions tend to underestimate the strain capacity of sections with circular hoops while overestimating it for sections confined with rectilinear hoops and double-headed crossies.

Figure 3.11 illustrates the experimental data (solid bubbles) and analytical models (hollow bubbles). The horizontal axis plots the transverse reinforcement ratio, ρ_c , while the vertical axis shows the drift ratio at the ultimate displacement Δ_{80} . Specimens and models with similar configurations share the same symbol color. Specimens with rectangular core, confined with rectilinear stirrups and crossies, are shown in blue; Specimens with circular hoops and a circular confined core, or models with cross section S, are in green; Specimens and models with a circular core and hollow section are shown in yellow; and specimens with square confined cores using rectilinear perimeter hoops and double-headed crossies, or models with cross section type H, are shown in red. Each bubble is labeled next to it with the Specimen number. The bubble areas are proportional to the axial load ratio of said specimen.

The analytical model data aligns with experimental findings, showing that increasing axial force decreases drift ratio capacity, regardless of cross-section geometry and transverse reinforcement configuration. Sections with circular hoop reinforcement and closer spacing achieved slightly larger drift ratios than those with larger spacing between hoops, even if the volumetric confinement ratio was lower, as seen in Specimen 6 compared to Model 11. Specimen 6 had a s/d_b ratio equal to 3.2 and a ρ_c of 0.008, while Model 11 had a s/d_b ratio of 4.8 and a ρ_c equal to 0.010. Despite Specimen 6 closer spacing (s/d_b ratio of 3.2 and ρ_c of 0.008), Model 11 (s/d_b ratio of 4.8 and ρ_c of 0.010) also performed well in terms of ultimate drift and ductility capacity. For sections with a void reinforced by a steel pipe, a similar performance to a gross cross section can be expected as long as the circular hoop reinforcement quantity, spacing, and neutral axis depth are consistent.

Increasing the volume of circular or headed cross-tie transverse reinforcement with well-restrained longitudinal bars leads to a nearly proportional increase in deformation capacity. Model 18 projects the expected behavior of Specimen 8 under larger displacements, allowing for determining a drift ratio for Δ_{80} . The imposed displacement protocol limited model 17 ultimate displacement capacity. Since it did not show significant moment capacity loss at the end of the simulation, it is reasonable to assume higher drift ratios can be achieved with this transverse reinforcement configuration, following the observed trend.

All proposed models and experimental specimens achieved a ductility capacity greater than 3.0, meeting the Caltrans requirement for Ordinary Standard Bridges.

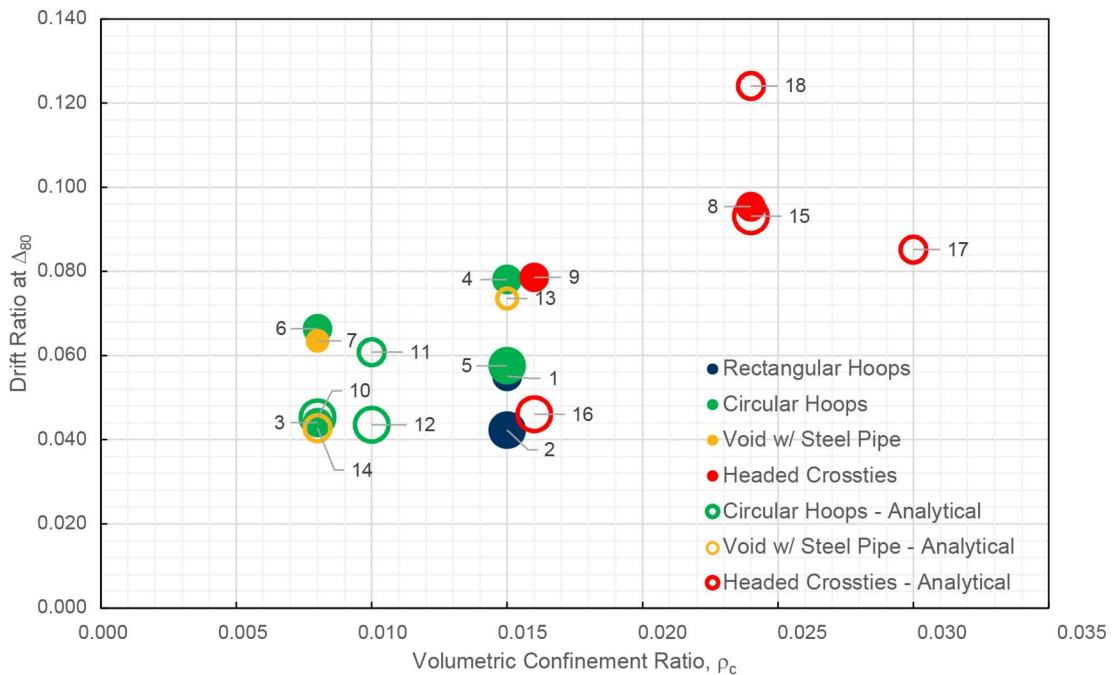


Figure 3.11. Volumetric confinement Ratio - Drift Ratio Relationship.

Using the data obtained from the experimental tests and parametric models, two expressions are proposed to estimate the ultimate drift capacity of an arch rib given a volumetric confinement ratio and axial force ratio. The ultimate drift capacity, δ_{80} , is the drift capacity the arch rib is expected

to achieve at a 20% loss of the maximum moment capacity. In other words, δ_{80} is the drift ratio at displacement Δ_{80} .

Equation (3.11) is proposed to calculate the ultimate drift capacity of an arch rib with a square cross section and a circular confined core achieved with circular hoops.

$$\delta_{80} = 2.25\rho_c - 0.85\frac{P}{f'_c A_g} + 0.06 \quad (3.11)$$

Table 3.11 presents the test specimens and numerical models with the same geometry as the Shasta Viaduct Replacement Bridge. It includes the volumetric confinement ratio ρ_c , the axial force ratio $P/A_g f'_c$, and the ultimate drift capacity, δ_{80} , obtained from experimental testing or analytical modeling. Using Equation (3.11), a predicted δ_{80} was calculated, with residuals shown. Equation (3.11) overestimates the ultimate drift capacity of Specimen 3, which had an unacceptable unrestrained longitudinal bar ratio, by 25%. For other specimens with acceptable bar ratios, the prediction for δ_{80} is adequate.

Table 3.11. Experimental or analytical ultimate displacement drift versus predicted ultimate displacement drift for sections with circular confinement.

Specimen or Model	ρ_c	$P/A_g f'_c$	Obtained δ_{80}	Predicted δ_{80}	Residuals
3	0.008	0.25	0.044	0.058	-0.014
4	0.015	0.25	0.078	0.074	0.004
5	0.015	0.40	0.058	0.061	-0.004
6	0.008	0.25	0.066	0.058	0.008
10	0.008	0.40	0.052	0.045	0.007
11	0.010	0.25	0.065	0.063	0.002
12	0.010	0.40	0.047	0.050	-0.003

Equation (3.12) is proposed to calculate the ultimate drift capacity of an arch rib with a square cross section reinforced with square stirrups and double-headed crossties as transverse reinforcement.

$$\delta_{80} = 1.60\rho_c - 0.10\frac{P}{f'_c A_g} + 0.08 \quad (3.12)$$

Table 3.12 presents sections reinforced with square hoops and double-headed crossties, along with the volumetric confinement ratio and axial load ratio. The obtained δ_{80} from experimental data or analytical models is shown next to the predicted δ_{80} using Equation (3.12). Residuals represent the difference between the obtained and predicted δ_{80} . Test specimens show good agreement with the

proposed equation, while analytical models display more variability. Additional analytical models can help develop an expression that results in more consistent predictions.

Table 3.12. Experimental or analytical ultimate displacement drift versus predicted ultimate displacement drift for sections with square confinement and double-headed bars crossties.

Specimen or Model	ρ_c	$P/A_g f'_c$	Obtained δ_{80}	Predicted δ_{80}	Residuals
8	0.025	0.25	0.095	0.098	-0.003
9	0.016	0.25	0.079	0.084	-0.006
15	0.024	0.40	0.093	0.082	0.011
16	0.016	0.40	0.059	0.069	-0.011
17	0.030	0.25	0.085	0.106	-0.022
18	0.024	0.25	0.124	0.097	0.027

3.9 Conclusions

In conclusion, the experimental investigation and subsequent finite-element modeling using OpenSees have provided a more robust insight into the seismic behavior of reinforced concrete arch ribs. Key findings from this study include:

1. The displacement-based fiber beam-column element in OpenSees effectively simulates the seismic response of reinforced concrete arch ribs, accurately capturing behaviors such as initial stiffness, yield, and ultimate strength, the general pattern of strength degradation, and maximum deformation capacity.
2. The fiber material models for steel and concrete were calibrated against laboratory test data to ensure the accuracy of the analytical models. Analytical expressions to estimate the maximum strain capacity of confined concrete can underestimate the strain capacity for sections confined with circular hoops or overestimate the strain capacity for sections with rectilinear transverse reinforcement and double-headed crossties.
3. Increasing the volume of transverse reinforcement produces a proportional increment in the section's deformation capacity. Hollow sections with a 0.6 D_i/D ratio, reinforced with steel pipe, have similar drift capacities to solid sections, given the same reinforcement configuration and neutral axis depth.
4. An increment in axial force reduces the displacement capacities of the sections in comparison to identical sections subjected to lower axial forces.
5. Specimens with a volumetric confinement ratio equal to or higher than 0.008 present a ductile behavior as long as the longitudinal bar buckling restraint ratio (s/d_b) does not exceed 4.8.
6. All experimental specimens and analytical models achieved ductility capacities exceeding 3.0, meeting Caltrans's seismic design criteria for Ordinary Standard Bridges.

7. Two new expressions are suggested to calculate the ultimate drift capacity, δ_{80} , of a reinforced concrete arch rib according to the transverse reinforcement configuration. These expressions are a function of the volumetric confinement ratio and axial force ratio.

In summary, the combined experimental and numerical approach has provided a robust framework for understanding and improving the seismic performance of reinforced concrete arch ribs. Further research could explore additional parameters or refine the proposed models (for example, use force-based fiber beam-column element in OpenSees).

3.10 Bibliography

- [1] Caltrans, *Caltrans Seismic Design Criteria v. 2.0*. California Department of Transportation, Tech. Rep., 2019.
- [2] F. McKenna, M. H. Scott, and G. L. Fenves, “Nonlinear Finite-Element Analysis Software Architecture Using Object Composition,” *Journal of Computing in Civil Engineering*, vol. 24, no. 1, pp. 95–107, Jan. 2010, doi: 10.1061/(ASCE)CP.1943-5487.0000002.
- [3] G. Benzoni, T. Ohtaki, M. J. N. Priestley, and F. Seible, “SEISMIC PERFORMANCE OF CIRCULAR REINFORCED CONCRETE COLUMNS UNDER VARYING AXIAL LOAD,” Art. no. UCSD/SSRP-96/04, Aug. 1996, Accessed: Jun. 11, 2024. [Online]. Available: <https://trid.trb.org/View/478610>
- [4] K. J. Elwood and M. O. Eberhard, “Effective Stiffness of Reinforced Concrete Columns,” *SJ*, vol. 106, no. 4, pp. 476–484, Jul. 2009, doi: 10.14359/56613.
- [5] AASHTO, *AASHTO LRFD Bridge Design Specifications, 9th Edition*. American Association of State Highway and Transportation Officials (AASHTO), 2020.
- [6] D. J. Miller, “Ductile Behavior of Reinforced Concrete Arch Ribs,” UC Berkeley, 2019.
- [7] A. Neuenhofer and F. C. Filippou, “Evaluation of Nonlinear Frame Finite-Element Models,” *Journal of Structural Engineering*, vol. 123, no. 7, pp. 958–966, Jul. 1997, doi: 10.1061/(ASCE)0733-9445(1997)123:7(958).
- [8] M. H. Scott and G. L. Fenves, “Plastic Hinge Integration Methods for Force-Based Beam–Column Elements,” *Journal of Structural Engineering*, vol. 132, no. 2, pp. 244–252, Feb. 2006, doi: 10.1061/(ASCE)0733-9445(2006)132:2(244).
- [9] J. Coleman and E. Spacone, “Localization Issues in Force-Based Frame Elements,” *Journal of Structural Engineering-asce - J STRUCT ENG-ASCE*, vol. 127, Nov. 2001, doi: 10.1061/(ASCE)0733-9445(2001)127:11(1257).
- [10] S. Popovics, “A numerical approach to the complete stress-strain curve of concrete,” *Cement and Concrete Research*, vol. 3, no. 5, pp. 583–599, Sep. 1973, doi: 10.1016/0008-8846(73)90096-3.
- [11] J. B. Mander, M. J. N. Priestley, and R. Park, “Theoretical Stress-Strain Model for Confined Concrete,” *Journal of Structural Engineering*, vol. 114, no. 8, pp. 1804–1826, Aug. 1988, doi: 10.1061/(ASCE)0733-9445(1988)114:8(1804).
- [12] F. E. Richart, A. Brandtzaeg, and R. L. Brown, *A Study of the Failure of Concrete Under Combined Compressive Stresses*. University of Illinois, 1928.
- [13] M. J. N. Priestley, F. Seible, and G. M. Calvi, *Seismic Design and Retrofit of Bridges*. John Wiley & Sons, Inc., 1996.
- [14] B. D. Scott, R. Park, and M. J. N. Priestley, “Stress-Strain Behavior of Concrete Confined by Overlapping Hoops at Low and High Strain Rates,” *JP*, vol. 79, no. 1, pp. 13–27, Jan. 1982, doi: 10.14359/10875.

- [15] J. Moehle, *Seismic Design of Reinforced Concrete Buildings*. McGraw-Hill Education, 2015.
- [16] S. Kunnath, Y. Heo, and J. Mohle, “Nonlinear Uniaxial Material Model for Reinforcing Steel Bars,” *Journal of Structural Engineering-asce - J STRUCT ENG-ASCE*, vol. 135, Apr. 2009, doi: 10.1061/(ASCE)0733-9445(2009)135:4(335).
- [17] A. Gomes and J. Appleton, “Nonlinear cyclic stress-strain relationship of reinforcing bars including buckling,” *Engineering Structures*, vol. 19, no. 10, pp. 822–826, Oct. 1997, doi: 10.1016/S0141-0296(97)00166-1.
- [18] D. Lehman, J. Moehle, S. Mahin, A. Calderone, and L. Henry, “Experimental Evaluation of the Seismic Performance of Reinforced Concrete Bridge Columns,” *Journal of Structural Engineering*, vol. 130, no. 6, pp. 869–879, Jun. 2004, doi: 10.1061/(ASCE)0733-9445(2004)130:6(869).
- [19] FEMA, *Interim protocols for determining seismic performance characteristics of structural and nonstructural components through laboratory testing: FEMA 461*. FEMA, Tech. Rep., 2007.
- [20] ASCE/SEI 41-17, *Seismic Evaluation and Retrofit of Existing Buildings*,. American Society of Civil Engineers, 2017. doi: 10.1061/9780784414859.
- [21] R. P. Dhakal and K. Maekawa, “Modeling for Postyield Buckling of Reinforcement,” *Journal of Structural Engineering*, vol. 128, no. 9, pp. 1139–1147, Sep. 2002, doi: 10.1061/(ASCE)0733-9445(2002)128:9(1139).

Chapter 4

Risk Analysis of Reinforced Concrete Arch Ribs

4.1 Introduction

In regions prone to significant seismic activity, such as California, arch bridges are expected to experience seismic events throughout their lifespan. It is crucial for engineers to understand the dynamic behavior and performance of arch bridges under seismic loading to ensure safety and functionality for predefined hazard levels.

The Seismic Design Criteria (SDC) [1], developed by the California Department of Transportation (Caltrans), establish seismic performance criteria for all bridges in California. The SDC defines two primary hazard evaluation levels. The first is the Functional Evaluation Earthquake (FEE), representing relatively small magnitude events that may occur multiple times during the bridge's lifespan, with a seismic hazard design spectrum based on a 20% probability of exceedance in 50 years (225-year return period). The second is the Safety Evaluation Earthquake (SEE), which has a lower probability of occurring during the bridge's life, characterized by a 5% probability of exceedance in 50 years (975-year return period). Each bridge category (Ordinary, Recovery, and Important) is assigned an expected post-earthquake damage state and service level based on the seismic hazard level. While the classification of arch bridges is not explicitly defined, they are typically considered Ordinary. Collapse prevention is the target performance for Ordinary bridges at the SEE hazard level. This chapter presents a framework to perform a risk analysis of a reinforced concrete arch rib using the Conditional Site Spectrum (CSS) methodology to select the ground motions.

4.2 Literature Review

Miller [2] presents a study on an analytical model of an archetypal arch bridge based on the Shasta Viaduct Replacement. The model was designed to replicate the prototype bridge while being generalized into an idealized form to overcome additional complexities unique to the Shasta Viaduct bridge. The study aimed to investigate the general behavior of arch bridges rather than focusing exclusively on the Shasta Viaduct Replacement. Miller performed a series of nonlinear pushover analyses, which provided valuable insights into the formation of plastic hinges in an arch rib bridge. Additionally, the study found that a large number of modes are required to achieve a high level of mass participation under dynamic loading.

A limitation of nonlinear pushover analysis is its inability to accurately replicate demands under actual earthquake loading. To overcome these limitations, an alternative nonlinear dynamic analysis method, such as Nonlinear Response History Analysis (NRHA), can be performed using a suite of representative site-specific ground motions for a determined hazard level and fundamental period. Nonlinear dynamic analysis can also help establish probabilistic fragility curves, which are useful in the context of Performance-Based Earthquake Engineering (PBEE).

Fragility Function Development Methodologies

A common method for performing nonlinear dynamic analysis to estimate fragility functions is the Incremental Dynamic Analysis (IDA) proposed by Vamvatsikos and Cornell [3]. This method involves subjecting an analytical model to a selected suite of ground motions that are scaled progressively, performing an individual Response History Analysis (RHA) for each scaling factor for a given ground motion. The ground motions are scaled by selecting an intensity measure (IM) that can predict in an accurate way the structure's seismic response. The scaling factors for the ground motions are incremented until the model reaches collapse or another defined engineering demand parameter (EDP) is reached. Each RHA results in an IM with a corresponding EDP. IDA curves can then be determined for each ground motion, typically using the pseudo-acceleration response at the first mode, with 5% damping, $S_a(T_1, 5\%)$, as the IM and any EDP of interest (i.e. peak drift ratio). The proportion of collapses (or exceeded EDPs) for a certain IM to the total number of ground motions is calculated, and a normal cumulative distribution function is fitted to obtain the empirical fragility function. Typically, the IM is incremented until the EDP of interest is exceeded for all ground motions.

However, the IDA methodology has a significant limitation. Scaling the IM of ground motions to extreme levels may produce unrealistic spectral shapes [4]. When ground motions are scaled to higher intensity levels, the characteristics of the ground motions, such as frequency content and duration, can change significantly from those of the original records. This can lead to unrealistic representations of seismic demands that are not consistent with the selected hazard level.

An alternative method that does not require ground motion scaling and is hazard-consistent is the Multiple Stripes Analysis (MSA) [5], [6]. In a Multiple Stripes Analysis, discrete levels of IM are defined, and a set of ground motions are selected for each IM. Unlike IDA, different ground motions can be selected for each discrete IM level. This presents an advantage over IDA because the ground motion records can be selected to match the spectral shape of each target intensity more accurately. However, a limitation of MSA compared to IDA is that the largest IM level might not produce a full set of Engineering Demand Parameter (EDP) values exceeding the EDP of interest (i.e., not all ground motions induce structural collapse), complicating the fitting of the fragility curve. To address this, Baker [5] proposed an efficient methodology to accurately fit data obtained from MSA into fragility curves.

Conditional Scenario Spectra

The Conditional Scenario Spectra (CSS) can be considered as a type of MSA. The CSS includes sets of realistic earthquake spectra with specified rates of occurrence that accurately represent the seismic hazard at a site across various hazard levels for a period of interest. Arteta and Abrahamson [7] provide a detailed procedure for estimating the CSS; a summary of the steps to perform a CSS is presented here:

1. For each specific hazard level, sets of candidate ground motion recordings are selected based on the site hazard disaggregation (M, R) for a period T_0 .
2. Target Uniform Hazard Spectra (UHS) are developed for several rates of exceedance representing the hazard level of interest.

3. Using the midpoint between consecutive UHS as hazard level, a Conditional Mean Spectrum (CMS) is computed conditioned to a period T_0 . By using the CMS in the ground motion selection, the spectral shape for each hazard level is guaranteed to be respected.
4. From the candidate recording set, subsets of ground motions are selected and scaled to match the CMS (± 2.5 standard deviations). The subset with the best fit to the CMS and its variability for a period T_0 (or period range) is selected using Monte Carlo simulation.
5. A rate of occurrence for each ground motion record is calculated and then optimized so the hazard produced by the selected scaled subset matches as closely as possible the hazard obtained from the Probabilistic Seismic Hazard Analysis (PSHA).

With the set of ground motions records selected using the CSS methodology for different hazard levels, it is possible to develop fragility curves for the EDPs of interest. An additional advantage of CSS is that, by using the rate of occurrence, it is possible to estimate the risk of the EDPs using structural-response hazard curves.

Performance Based Earthquake Engineering (PBEE)

Fragility curves are an important part of the Performance Based Earthquake Engineering (PBEE) methodology developed by the Pacific Earthquake Engineering Research Center (PEER). This method was created to assess structural performance with a probabilistic approach, accounting for uncertainties such as seismic hazard, structural response, damage levels, and losses. The PEER PBEE methodology aims to provide stakeholders with meaningful and quantitative measurements (called Decision Variables) to assess the performance of a structure and achieve specified performance targets.

The PBEE framework presented by Moehle and Deierlein [8] consists of four analysis stages for a given facility, described below. Figure 4.1 presents a flow diagram for the PEER PBEE framework.

1. *Seismic Hazard Analysis.* Considering the probability of the seismic events in the nearby region, a PSHA determines the mean annual rate of exceedance for a given intensity measure, $\lambda(im)$, is determined. Results from this analysis include hazard curves showing the variation on the selected IM and suites of ground motion records.
2. *Structural Response Analysis.* A structural analytical model of the facility is subjected to the IM. Engineering demand parameters (EDPs) are obtained from running, typically nonlinear time-history analysis. The structural analysis output is the probability of exceedance an EDP given a IM level, $G(edp | im)$. Common EDPs are drift ratios, stresses, or floor acceleration (for non-structural components).
3. *Damage Analysis.* The damage analysis estimates the level of physical damage on the structure through previously established Damage Measurements (DM). Fragility functions model the probability of a DM and are usually obtained with experimental tests. The damage analysis provides the probability of exceeding a DM given different levels of EDP, $G(dm | edp)$. Cracking, spalling, or collapse are examples of Damage Measurements.
4. *Loss Analysis.* In this analysis, the probability of exceeding a Decision Variable (DV) given different DM levels, $G(dv | dm)$ is calculated. These decision variables could be fatalities,

economic loss, repair duration or injuries. The probability of exceeding a certain level of DV, $\lambda(DV)$, can be computed using Equation (4.1) to achieve a desirable target performance.

$$\lambda(DV) = \int \int \int G(DV | DM) \cdot dG(DM | EDP) \cdot dG(EDP | IM) \cdot |d\lambda(IM)| \quad (4.1)$$

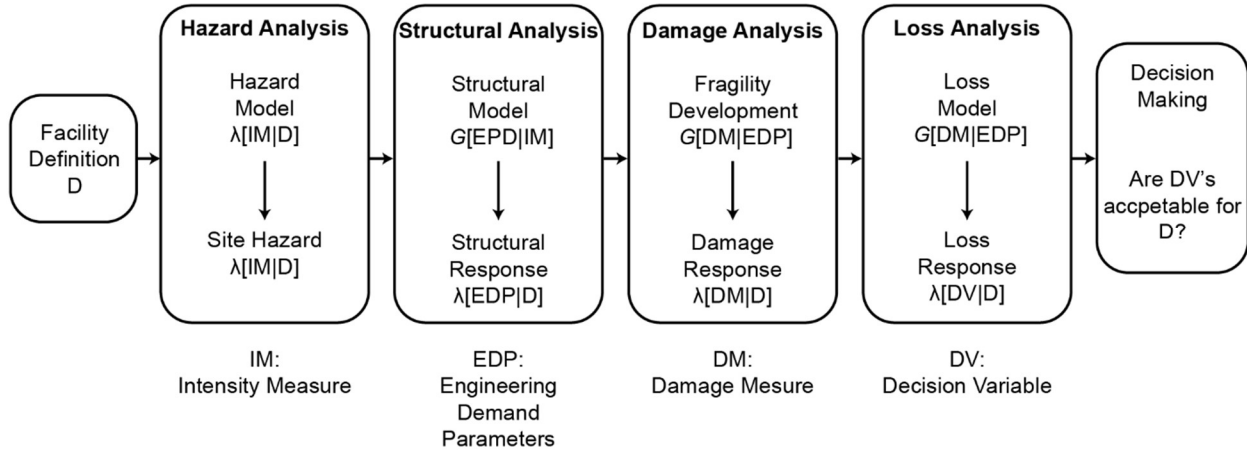


Figure 4.1. Overview of the PEER PBEE framework (Adapted from Porter [9]).

Probabilistic Damage Control Application (PDCA)

The Probabilistic Damage Control Application (PDCA) (see [9] and [10]) is an implementation of performance-based earthquake engineering applied to the seismic design of bridge columns. Similar to PBEE, PDCA enables targeting specific performance levels in highway bridges based on a given damage state. This approach provides engineers and owners with the necessary information to evaluate the safety and economic implications of the structure over its lifespan.

PDCA utilizes a Damage Index (DI) as the engineering response parameter. The DI quantifies the damage level as a function of the column lateral displacement. Vosooghi *et al.* [10] defined six damage states (DS) based on visual inspection of experimental tests. The defined damage states are DS-1 (flexural cracks), DS-2 (minor concrete spalling), DS-3 (extensive concrete spalling or extensive shear cracks), DS-4 (visible bars), DS-5 (imminent failure, damage in concrete core, or damage in longitudinal bar reinforcement) and DS-6 (failure).

With the damage states defined, the DI are correlated to any DS of interest and “fragility curves” are developed. These fragility curves are then used to estimate the probability of exceeding a DS of interest given a hazard level.

4.3 Methodology for Risk Analysis on Arch Bridges

A brief methodology to explore the dynamic behavior and perform a risk analysis on arch bridges is described below. This approach suggests using Conditional Scenario Spectra to obtain hazard-consistent ground motions that induce demands from the elastic range, through the inelastic range,

up to collapse, assigning occurrence rates to said ground motions based on their spectral shape and intensity.

1. Obtain the dynamic properties of the arch bridge of interest. Use a numerical model in OpenSees, such as the archetypal bridge developed by Miller, to determine dynamic properties (e.g., fundamental period, modal shapes, effective mass participation) of a reinforced concrete arch bridge.
 - 1.1. While the arch rib numerical model can be used for a NRHA, the complexity of the full bridge model may be computationally expensive. Alternatively, use a simpler, more efficient model. An equivalent Single Degree of Freedom (SDOF) system with effective modal mass, M_n^* , and effective modal height, h_n^* , corresponding to the n th mode, can be used as an alternative model. As shown in Figure 4.2, the SDOF model element consists of a lumped mass at the top, M_n^* , a height h_n^* , a stiffness, k , and damping coefficient, ζ . The element cross-section can be modeled using the validated analytical models presented in the previous chapter.

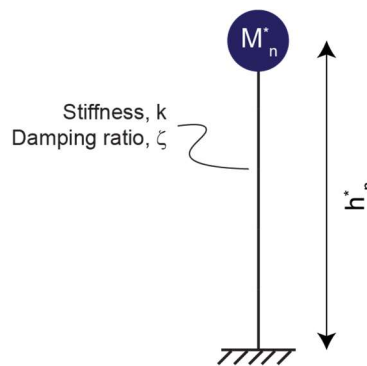


Figure 4.2. SDOF system with effective modal mass and effective modal height for the n th mode.

2. Site selection. In this case, the Shasta Viaduct Replacement Bridge is located in Northern California (40.77, -122.31). The seismic hazard in this region is primarily governed by the Cascadia subduction zone, which tends to produce seismic events with larger magnitudes than crustal regions. The intention of this framework is to understand the general dynamic behavior of an arch rib section under seismic loading rather than focusing specifically on the dynamic behavior of the Shasta Viaduct Bridge. Consequently, a site more representative of any arch bridge built in California might be selected.
3. Use the CSS methodology for selecting hazard-consistent ground motions. A brief summary of the CSS procedure is described below.
 - 3.1. Define Uniform Hazard Spectra (UHS) for a range of hazard levels.
 - 3.2. Perform Conditional Mean Spectra (CMS) using midpoints between consecutive UHS at a period of interest. Arteta *et al.* [11] suggest selecting ground motions near the elongated period (typically $1.5T_1$) for the largest median displacement.

- 3.3. Propose several sets of scaled ground motions to match the CMS.
- 3.4. Select the best-fitting set and optimize to obtain a recurrence period so the hazard from the selected scaled subset matches the Probabilistic Seismic Hazard Analysis (PSHA) hazard.

Figure 4.3 illustrates an example of a combined response spectra for different target UHS. These target UHS are shown using solid colored lines. The CMS are shown with colored broken lines, and the conditional period is indicated by a vertical broken line. The set of scaled ground motions used to match each CMS is shown in grayscale.

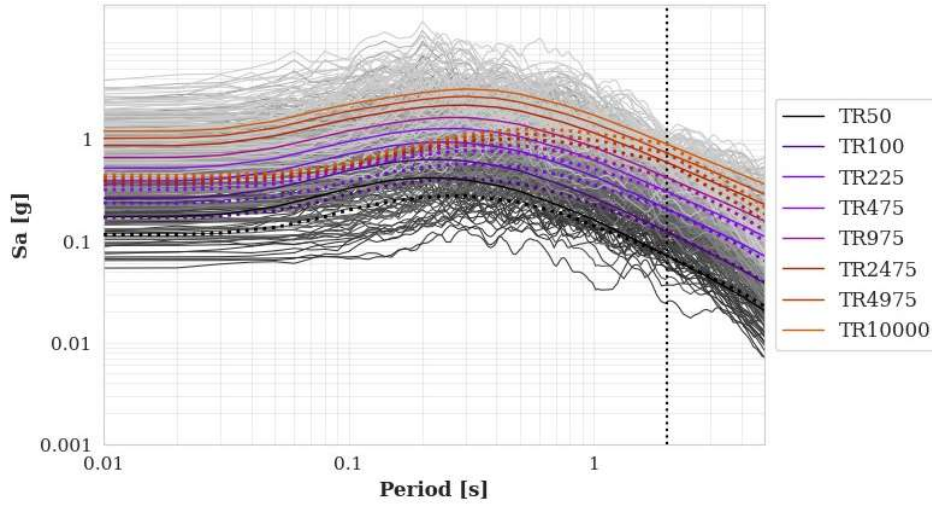


Figure 4.3. Combined Response Spectra for several Hazard Levels conditioned at T=2s. (Figure provided by Nicolas Quintero).

4. Obtain the structural response. Use the nonlinear equivalent SDOF model to perform a NRHA using the scaled set of selected ground motions to record the EDPs of interest.
5. Define Damage Measurements and develop fragility functions. The ultimate drift ratio obtained in Chapter 2 can be used as a “collapse” drift ratio. Fragility functions can be computed using the methodology proposed by Baker [5].
6. Compute EDP hazard curves $\lambda(edp)$, using Equation (4.2) where $v(EDP > d)$ represents the annual frequency at which the demand d is exceeded; the $Rate_{CSS,i}$ is the assigned rate of each time series; and $H(EDP-d)$ is the Heaviside function, which is 1 if the EDP from the series i exceeds the demand level d , and 0 otherwise.

$$\lambda(edp) \equiv v(EDP > d) = \sum_{i=1}^{\#recordings} Rate_{CSS,i} H(EDP - d) \quad (4.2)$$

Once the EDP hazard is calculated, it is possible to plot and determine the Return Period (inverse of the annual rate of exceedance) of a certain EDP level. This can be useful to establish whether the risk associated with demand level d is acceptable or not.

This methodology can be applied by assigning the cross sections studied in the experimental program. Understanding the dynamic behavior and risk analysis of each specimen's reinforcement helps assess the impact of transverse reinforcement detailing on seismic performance.

Additionally, it is suggested that we explore the impact of a large sacrificial cover on the seismic behavior in cross sections based on the Shasta Viaduct Replacement Bridge and investigate how the absence of such covers affects the dynamic behavior of reinforced concrete arch ribs.

4.4 Bibliography

- [1] Caltrans, *Caltrans Seismic Design Criteria v. 2.0*. California Department of Transportation, Tech. Rep., 2019.
- [2] D. J. Miller, "Ductile Behavior of Reinforced Concrete Arch Ribs," UC Berkeley, 2019.
- [3] D. Vamvatsikos and C. A. Cornell, "Incremental dynamic analysis," *Earthquake Engineering & Structural Dynamics*, vol. 31, no. 3, pp. 491–514, 2002, doi: 10.1002/eqe.141.
- [4] J. W. Baker and C. A. Cornell, "Vector-Valued Ground Motion Intensity Measures for Probabilistic Seismic Demand Analysis," *PEER Report 2006/08*, no. Pacific Earthquake Engineering Research Center.
- [5] J. W. Baker, "Efficient Analytical Fragility Function Fitting Using Dynamic Structural Analysis," *Earthquake Spectra*, vol. 31, no. 1, pp. 579–599, Feb. 2015, doi: 10.1193/021113EQS025M.
- [6] F. Jalayer and C. Cornell, "Alternative non-linear demand estimation methods for probability-based seismic assessments," *Earthquake Engineering & Structural Dynamics*, vol. 38, pp. 951–972, Jul. 2009, doi: 10.1002/eqe.876.
- [7] C. Arteta, "Conditional Scenario Spectra (CSS) for Hazard-Consistent Analysis of Engineering Systems," *Earthquake Spectra*, vol. 35, pp. 737–757, May 2019, doi: 10.1193/102116EQS176M.
- [8] J. Moehle and G. Deierlein, "A framework methodology for performance-based earthquake engineering," 2004. [Online]. Available: <https://www.semanticscholar.org/paper/A-framework-methodology-for-performance-based-Moehle-Deierlein/4249c3817f484024407cc893b633adc080b7b391>
- [9] Y. H. Yoon, S. Ataya, M. Mahan, A. Malek, M. S. Saiidi, and T. Zokaie, "Probabilistic Damage Control Application: Implementation of Performance-Based Earthquake Engineering in Seismic Design of Highway Bridge Columns," *Journal of Bridge Engineering*, vol. 24, no. 7, p. 04019068, Jul. 2019, doi: 10.1061/(ASCE)BE.1943-5592.0001443.
- [10] A. Vosooghi, A. Saini, and S. Saiidi, "Probabilistic Damage Control Approach for Seismic Design of Bridges," May 2013.
- [11] C. A. Arteta, A. Torregroza, D. Gaspar, and N. Abrahamson, "Sensitivity of the conditional period selection in the structural response using the CMS as target spectrum," *Earthquake Spectra*, vol. 38, no. 3, pp. 1844–1871, Aug. 2022, doi: 10.1177/87552930221081150.

Chapter 5

Summary and Conclusions

5.1 Summary

This dissertation examines the impact of high axial forces on the seismic behavior of reinforced concrete arch bridges. The main goals are to evaluate the effectiveness of different confinement reinforcement details in enhancing displacement capacity, assess the impact of high axial forces on drift capacity, and recommend detailing practices for earthquake-resistant design.

The experimental investigation involved constructing and testing nine one-third scale specimens based on prototypes from the Spanish Creek Replacement and Shasta Viaduct Replacement projects. The test specimens were constructed as straight elements representing critical regions of an arch rib. These specimens were subjected to constant axial compression and cyclic lateral displacements of increasing amplitudes to study the effects of the confinement reinforcement configurations, quantity, and detailing, as well as the effects of the axial load ratio.

The nine test specimen cross sections are described as follows. Specimens 1 and 2 had rectangular cores confined with rectilinear stirrups and crossties with 135-degree and 90-degree hooks. Specimens 3 to 6 consisted of rectangular cross sections with circular confined cores achieved with welded circular hoops, primary longitudinal reinforcement inside these hoops followed a circular array. Secondary U-shaped rectilinear hoops were lap-spliced to form a continuous hoop containing the cross section corners. Specimen 7, similar to Specimens 3 to 6, included a hollow section with a 406 mm diameter steel pipe, designed to resist core concrete dilation without contributing to moment resistance during testing. Specimens 8 and 9 had square confined cores with rectilinear perimeter hoops and double-headed crossties. Table 5.1 shows a summary of the main characteristics of the experimental program, including the cross section geometries, concrete compressive strength at the day of testing f'_c , volumetric confinement ratio ρ_c , transverse reinforcement spacing, longitudinal bar buckling restrain ratio s/d_b , longitudinal reinforcement ratio ρ_l , axial force P applied during testing, and axial load ratio $P/A_g f'_c$.

Results, including hysteretic moment-drift relationships, demonstrated that all specimens met or exceeded the ductility requirements for seismic design in California, with increased transverse confinement significantly boosting seismic performance in terms of displacement ductility and moment capacity.

Subsequently, analytical models were developed and validated using OpenSees to further examine the impact of varying critical parameters, such as axial load, volumetric confinement ratio, and longitudinal bar buckling restraining ratio. These models, calibrated against experimental data, effectively simulated the seismic response of reinforced concrete arch ribs and provided a robust dataset that complements the experimental findings.

Finally, a methodology to investigate the dynamic behavior of arch rib sections derived from the Shasta Viaduct Replacement Bridge is presented. Conditional Site Spectrum (CSS) methodology is suggested to select ground motions.

Table 5.1. Summary of properties and details of test specimens.

Specimen	Cross Section	f'_c , MPa [ksi]	ρ_c	s, mm [in]	s/ d_b	ρ_l	P, kN [kips]	P/ $A_g f'_c$
1		31.1 [4.51]	0.015	76.2 [3]	4.8	0.014	6010 [1350]	0.25
2		40.0 [5.80]	0.015	76.2 [3]	4.8	0.014	11500 [2590]	0.40
3		34.5 [5.01]	0.008	101.6 [4]	6.4	0.011	4340 [975]	0.25
4		39.4 [5.71]	0.015	50.8 [2]	3.2	0.011	4870 [1100]	0.25
5		33.0 [4.79]	0.015	50.8 [2]	3.2	0.011	6650 [1500]	0.40
6		29.9 [4.34]	0.008	50.8 [2]	3.2	0.011	3780 [850]	0.25
7		29.4 [4.26]	0.008	50.8 [2]	3.2	0.011	2450 [550]	0.16
8		33.1 [4.80]	0.024	50.8 [2]	3.2	0.013	3020 [680]	0.25
9		33.1 [4.80]	0.016	76.2 [3]	4.8	0.013	3020 [680]	0.25

5.2 Conclusions

Experimental Program

The experimental program aimed to understand the impact of high axial forces and different reinforcement detailing configurations on the seismic performance of reinforced concrete arch bridges. Prototypes from the Spanish Creek Replacement Bridge and the Shasta Viaduct Replacement Bridge were studied. The former consisted of a rectangular section reinforced with rectangular stirrups and hooked crossies, while the latter had a square section with a circular core confined with circular hoops. Nine one-third scale test specimens were constructed to closely mimic the prototypes but changing the parameters of interest: confinement method (including the section), the amount of transverse reinforcement and detailing, and axial force ratio.

The experimental program involved testing these specimens under constant axial compression and cyclic lateral displacements. The experimental key findings are as follows:

1. Impact of Axial Forces: Increasing axial force reduces the displacement capacity of arch bridge segments.
2. Reinforcement Detailing: Circular hoops outperformed rectilinear hoops in terms of displacement capacity, regardless of axial load ratio.
3. Volumetric transverse reinforcement: An increment in the volumetric transverse reinforcement produces a proportional increment in deformation capacity for any given configuration. Additionally, specimens with higher volumetric confinement ratios were able to achieve higher drift displacements before bar fracture.
4. Transverse reinforcement spacing: Closer transverse reinforcement spacing enhanced performance, with circular hoops and headed crossies achieving a desirable ductile behavior.
5. Buckling Restraint Ratios: Adequate restraint of longitudinal bars is critical for ductile behavior. Longitudinal bar buckling restraint ratios (s/d_b) higher than 4.8 presented a non-ductile behavior, suggesting this value is a threshold for achieving satisfactory ductile behavior.
6. Voided Sections: The presence of a void reinforced with a pipe does not significantly affect performance compared with any other circular hoop reinforced section, given the same reinforcement quantity, spacing, and neutral axis depth.

The damage progression observed across all specimens included initial cracking, yielding of longitudinal reinforcement, cover spalling, longitudinal bar buckling, transverse bar fracture, and longitudinal reinforcement fracture.

Analytical Parametric Study

A finite-element model of an arch rib section was developed using OpenSees. The model employed a displacement-based fiber beam-column element to replicate the experimental specimens. Calibration of the model was performed using experimental measured material properties and experimental data. The analytical model allowed for a parametric study, enhancing the dataset beyond the experimental findings. Key observations include:

1. The displacement-based fiber beam-column element in OpenSees successfully replicates the seismic response of reinforced concrete arch ribs.
2. Analytical expressions for estimating the ultimate confined concrete strain capacity can underestimate strain capacity for sections with circular hoops and overestimate it for sections with rectilinear transverse reinforcement and double-headed crossties.
3. Similar to the experimental findings, increasing the volumetric confinement ratio produces a proportional increment in displacement capacity of the section. Increment in axial force reduces the displacement capacities of the sections.
4. Specimens with volumetric confinement ratio equal or higher than 0.008 present a ductile behavior as long as the longitudinal bar buckling restraint ratio (s/d_b) does not exceed 4.8.
5. Both experimental specimens and analytical models achieved ductility capacities exceeding 3.0, meeting Caltrans SDC criteria for Ordinary Standard Bridges.

5.3 Design Recommendations

Based on experimental data and analytical models, the following recommendations are made for ensuring safe ductile behavior in bridge arch ribs:

1. The use of circular welded hoops as transverse reinforcement is recommended. Experimental data demonstrated that cross sections with circular hoops (as the Shasta Viaduct Bridge) can achieve superior displacement capacity levels.
2. The use of 90-degree and 135-degree hook crossties as transverse reinforcement is not recommended. Sections with these crossties, like those in the Spanish Creek Replacement Bridge, show issues at large displacements due to the opening of the 90-degree hook crossties, leaving longitudinal bars unsupported, leading to early bar buckling and loss of moment capacity.
3. The use of double-headed bars is suggested as an alternative to the 90-degree and 135-degree hook crossties. Their use showed to provide an efficient confinement and restrain to the longitudinal reinforcement at large lateral displacements. Strict quality control during construction is recommended. The use of J-bars should also be explored as alternative.
4. Elements under high axial forces were able to reach acceptable ductility levels and displacement capacities however, it is not recommended that the axial force exceeds $0.25A_g f'_c$. Higher axial forces reduce displacement capacity compared to sections under lower axial forces.
5. In order to increase displacement capacity in the element, it is recommended to increase the transverse reinforcement quantity.
6. Maintain a restraint ratio (s/d_b) of no more than 4.8. Ratios of 2.4 and 3.5, as used in the prototype bridges, are effective for ductile behavior.
7. Sections with a volumetric confinement ratio ≥ 0.008 and a longitudinal steel ratio ≥ 0.01 provide ductile behavior for sections reinforced with circular welded hoops.
8. Use of hollow sections with a steel pipe resulted effective however, some considerations have to be made to ensure a satisfactory behavior.
 - 8.1. The inside-to-outside diameter ratio should be less than 0.6.
 - 8.2. Avoid placing the neutral axis inside the void.
 - 8.3. The steel reinforcement must satisfy:
 - 8.3.1. Volumetric confinement ratio ≥ 0.008 .
 - 8.3.2. Longitudinal steel ratio ≥ 0.01 .
 - 8.3.3. Longitudinal bar buckling ratio (s/d_b) ≤ 3.2 .

The Shasta Viaduct Bridge design outperformed the Spanish Creek Replacement Bridge under high and moderate axial forces due to a higher transverse reinforcement ratio, which resulted in greater displacement capacities despite a higher s/d_b ratio. Circular confinement proved effective in restraining longitudinal bars.

Two expressions are proposed to estimate the ultimate drift capacity of an arch rib, δ_{80} , given a volumetric confinement ratio and axial force ratio.

Equation (5.1) is proposed to calculate the ultimate drift capacity of an arch rib with a square cross section and a circular confined core achieved with circular hoops.

$$\delta_{80} = 2.25\rho_c - 0.85\frac{P}{f'_c A_g} + 0.06 \quad (5.1)$$

Equation (5.2) is proposed to calculate the ultimate drift capacity of an arch rib with a square cross section reinforced with square stirrups and double-headed cross-ties as transverse reinforcement.

$$\delta_{80} = 1.60\rho_c - 0.10\frac{P}{f'_c A_g} + 0.08 \quad (5.2)$$

Appendix A.

A.1. Specimen Photographs

A.1.1. Specimen 5



(a) Cross section during construction.



(b) Column cage during construction.



(c) Foundation Block during construction.



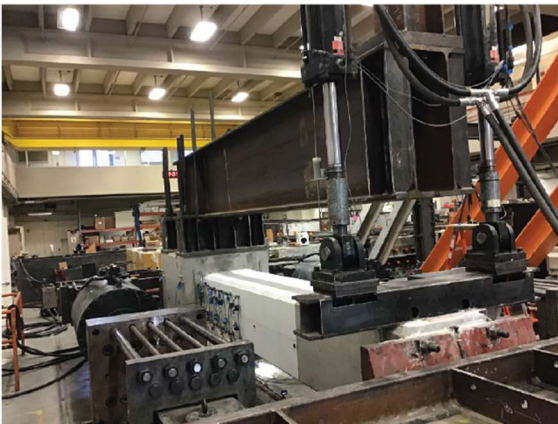
(d) Foundation Block during construction.



(e) Column-Foundation joint.



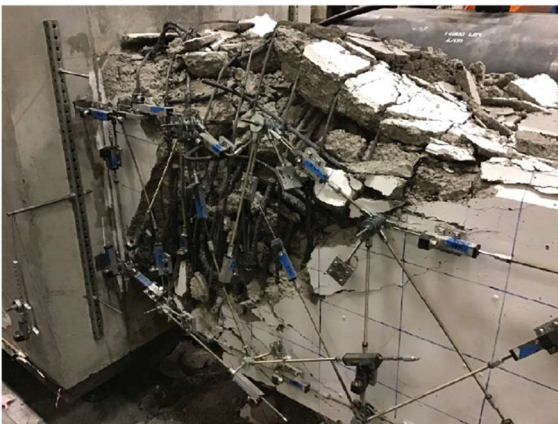
(f) Specimen prior to casting.



(g) Global configuration during test.



(h) Instrumentation during test.



(i) Instrumentation failure, post-testing.



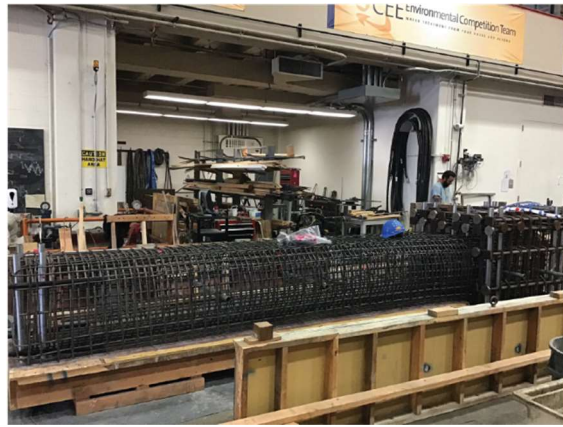
(j) Instrumentation failure post-testing.

Figure A.1.1. Specimen 5 photographs.

A.1.2. Specimen 6



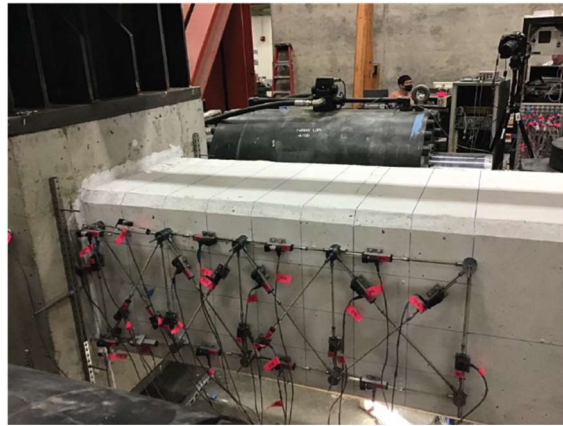
(a) Column cage during construction.



(b) Column cage during construction.



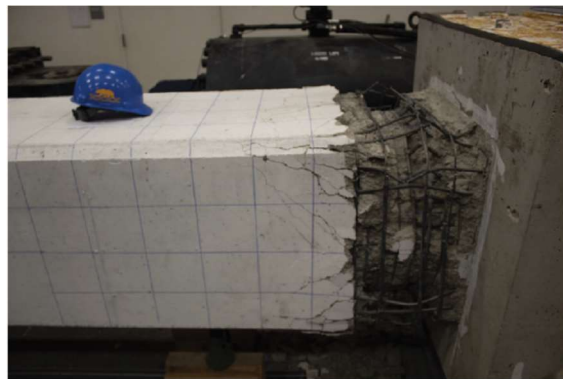
(c) Specimen prior to casting.



(d) Instrumentation during test.



(e) Post-testing column-foundation joint (south side).



(f) Post-testing column-foundation joint (north side).



(g) Post-testing column-foundation joint
(bottom face).



(h) Post-testing column-foundation joint
(top face).

Figure A.1.2. Specimen 6 photographs.

A.1.3. Specimen 7



(a) Column cage during construction.



(b) Column cage during construction with steel pipe.



(c) Pipe cap at the column tip.



(d) Specimen prior to casting.



(e) Post-testing column-foundation joint (south side).



(f) Post-testing column-foundation joint (north side).



(g) Instrumentation failure post-testing.



(h) Post-testing steel pipe damage.



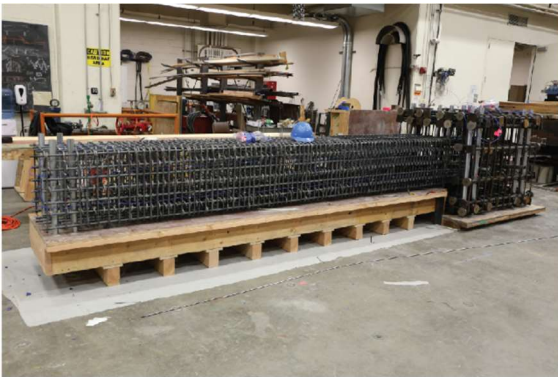
(i) Post-testing column-foundation joint (bottom face).



(j) Post-testing column-foundation joint (top face).

Figure A.1.3. Specimen 7 photographs.

A.1.4. Specimen 8



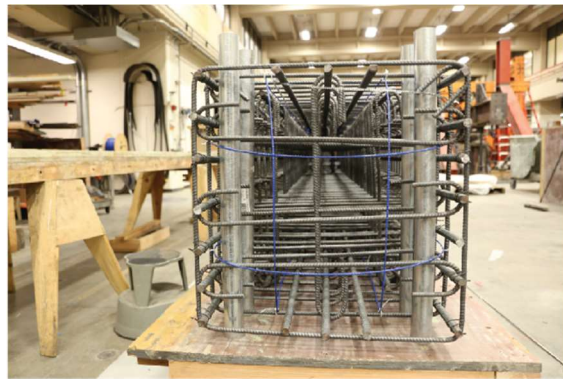
(a) Column cage during construction.



(b) Column cage during construction.



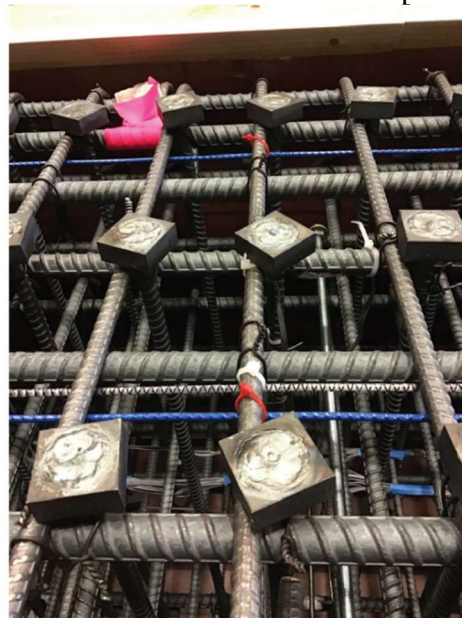
(c) Headed bars placement at column joint.



(d) Cross section during construction instrumented with fiber optics.



(e) Column Cage during construction.



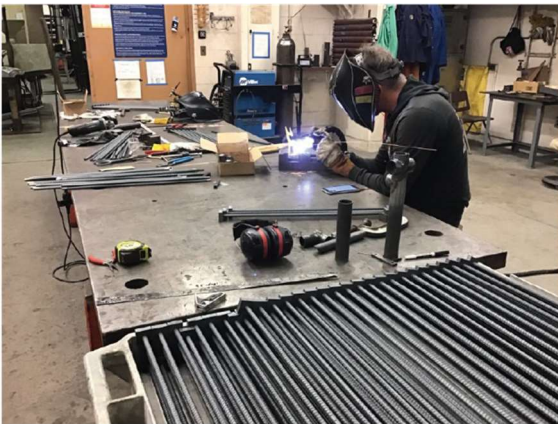
(f) Headed bars placement over transverse hoops.



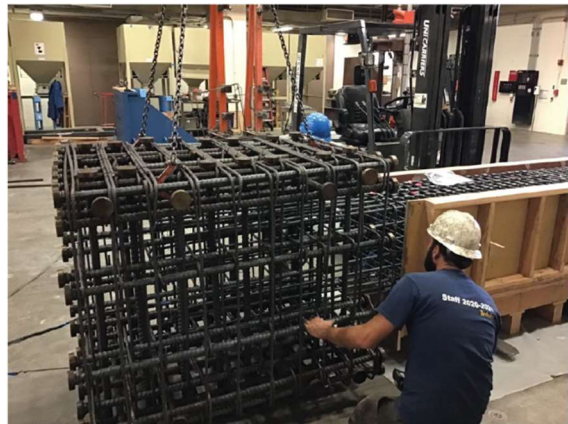
(g) Headed bars placement over hoops.



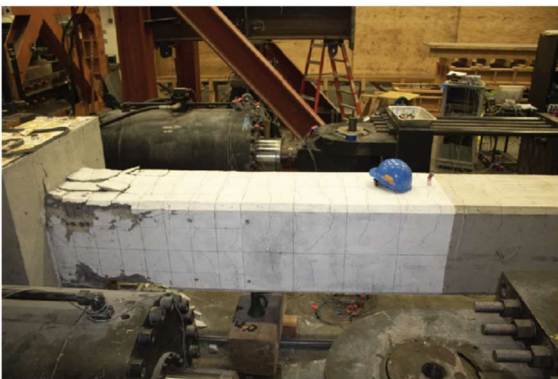
(h) Headed bars.



(i) Headed bars in-house fabrication.



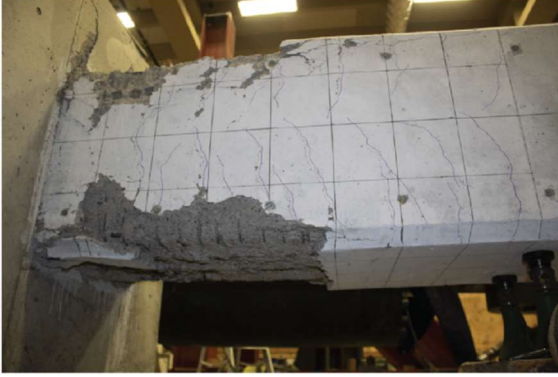
(j) Foundation Block.



(k) Post-testing column-foundation joint (south side).



(l) Post-testing column-foundation joint (north side).



(m) Post-testing column-foundation joint (south side).



(n) Post-testing column-foundation joint (north side).



(o) Post-testing column-foundation joint (bottom face).



(p) Post-testing column-foundation joint (top face).



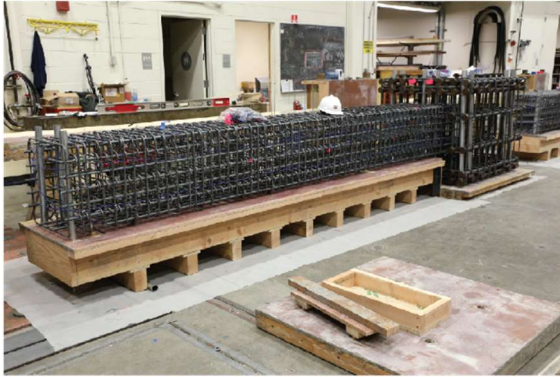
(q) Buckled transverse reinforcement.
Note that the headed bar is not providing an effective restraint on the hoop.



(r) Bar fracture between hoops.

Figure A.1.4. Specimen 8 photographs.

A.1.5. Specimen 9



(a) Column cage during construction.



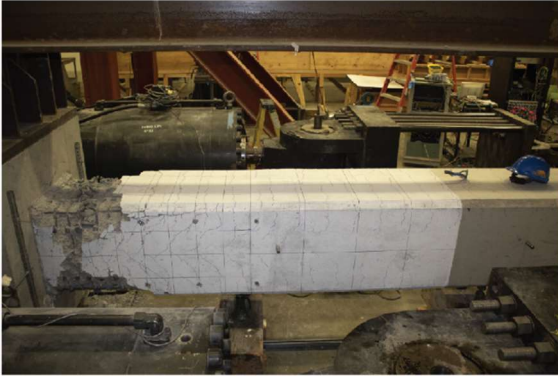
(b) Column cage during construction.



(c) Column cage during construction (top face).



(d) Headed bars placement over transverse hoops.



(e) Post-testing column-foundation joint (south side).



(f) Post-testing column-foundation joint (north side).



(g) Post-testing column-foundation joint (bottom face).



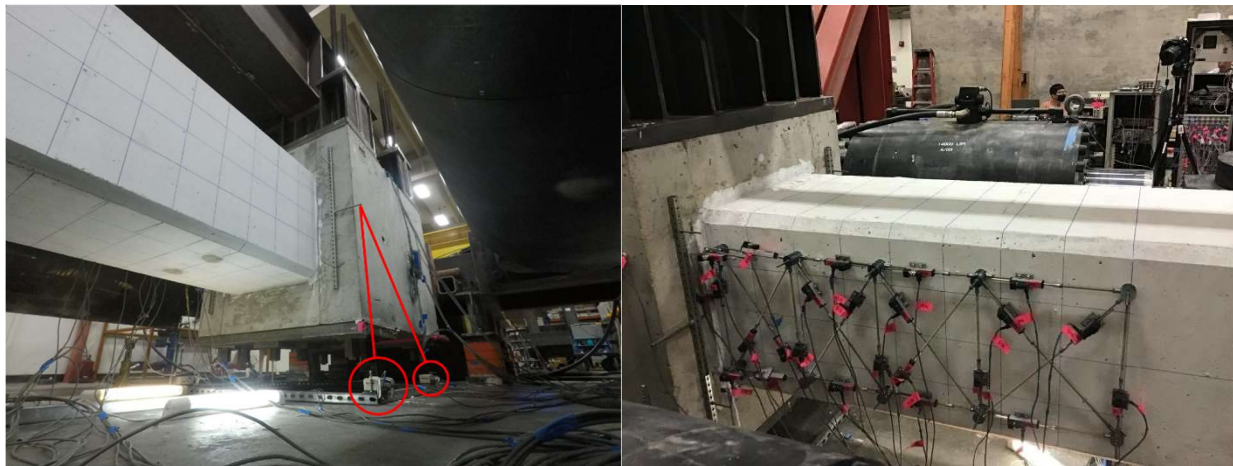
(h) Post-testing column-foundation joint (bottom face).

Figure A.1.5. Specimen 9 photographs.

Appendix B.

B.1. Instrumentation

During the experimental program, various instruments were employed to measure different types of deformations and strains in the specimens. String potentiometers were used to capture global displacements at the column base and column tip (see Figure B.1a). Strain gauges were applied to the reinforcement bars to monitor strains in both longitudinal and transverse reinforcements. A truss arrangement of LVDTs was utilized to decouple and measure flexural, shear, axial, and dilative deformations (see Figure B.1b). In later specimens, fiber optics were introduced to overcome the limitations of LVDTs, providing continuous strain profiles along the entire column length.



(a) String potentiometer at column base.

(b) Linear potentiometers on south face.

Figure B.1. Instrumentation photographs.

Global deformation

String potentiometers were installed to measure the global displacement at the column-foundation joint and the column tip (where the vertical load was applied). At both locations, two string potentiometers were installed on each side (see Figure B.2) to track and record displacements during the test. A tare measurement was taken before testing began. The recordings from each pair of potentiometers were triangulated to determine the coordinates of the column base or tip. The average measurement of both sides was taken for the analysis.

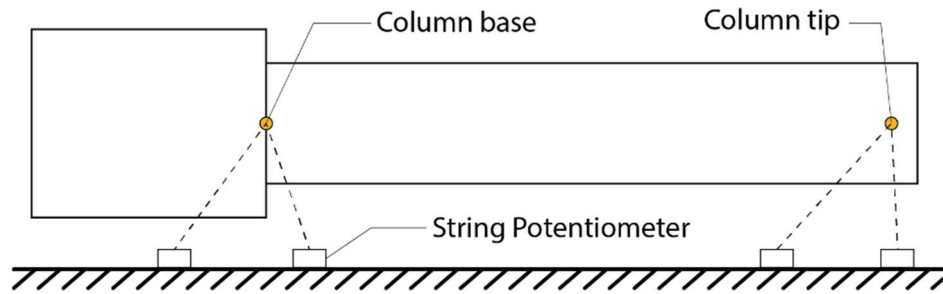


Figure B.2. Instrumentation for global deformations.

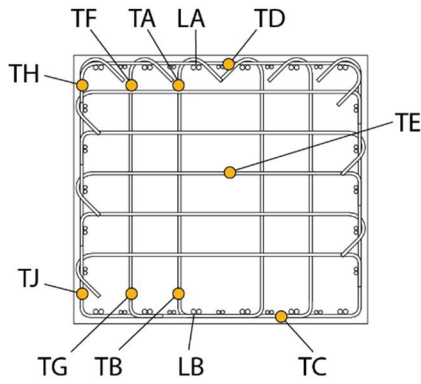
Reinforcement Strains

Strain gauges were used to measure the strain in the reinforcement bars. The top and bottom longitudinal bars were instrumented with gauges every half section depth ($0.5D$), starting from the column-foundation joint up to a distance of $2D$. These bars also had strain gauges within the foundation block (at $0.5D$ and $1.0D$ from the column-foundation joint).

Transverse reinforcement was instrumented with gauges approximately every $0.5D$ for the main transverse reinforcement (hoops or rectangular stirrups). Secondary transverse reinforcement, including cross-ties and steel pipe, when applicable, was also instrumented.

Figure B.3 shows the location of the gauges in each of the different cross sections. In this figure, the first character in the strain gauge (SG) nomenclature corresponds to the type of reinforcement being measured: “L” for longitudinal bars, “T” for transverse reinforcement, “P” for steel pipe, and “H” for headed cross-ties. The second character assigns a letter, starting from A, in alphabetical order, to indicate the instrument placement in the cross section. The location and gauge distribution along the column length are also displayed in tabular format.

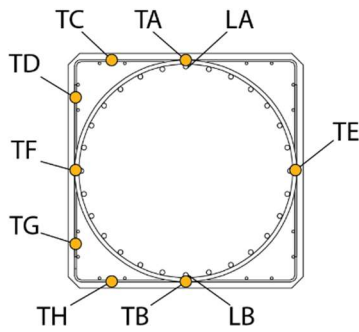
The gauges on the longitudinal bars were placed on the interior face of the bars (facing the core) to minimize damage during construction. The strain gauges on the transverse reinforcement were positioned to be in the same plane as the cross section (facing the column tip or foundation block, not the core).



Instrumented Cross Section	Location ^a	Longitudinal SG Placement	Transverse SG Placement
1	0	LA-LB	TA-TC
2	0.5D	LA-LB	TA-TJ
3	D	LA-LB	TA-TC
4	1.5D	LA-LB	TA-TE
5	2D	LA-LB	TA-TC

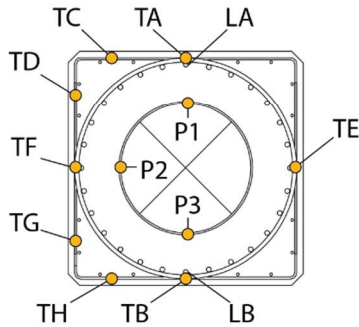
^a Nominal location measured from the column base.

(a) Specimen 1 and 2



Instrumented Cross Section	Location	Longitudinal SG Placement	Transverse SG Placement
1	0	LA-LB	TA-TB
2	0.5D	LA-LB	TA-TH
3	D	LA-LB	TA-TB
4	1.5D	LA-LB	TA-TD
5	2D	LA-LB	TA-TB

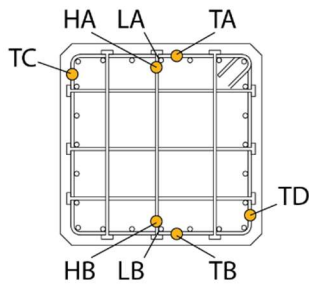
(b) Specimen 3 to 6



Instrumented Cross Section	Location	Longitudinal SG Placement	Transverse SG Placement ^a
1	0	LA-LB	TA-TB
2	0.5D	LA-LB	TA-TH
3	D	LA-LB	TA-TB
4	1.5D	LA-LB	TA-TD
5	2D	LA-LB	TA-TB

^a P1-P3 were placed at 0 in, 16 in, and 32in. measured from the column base.

(c) Specimen 7



Instrumented Cross Section	Location	Longitudinal SG Placement	Transverse SG Placement ^a
1	0	LA-LB	TA-TB
2	0.5D	LA-LB	TA-TD
3	D	LA-LB	TA-TB
4	1.5D	LA-LB	TA-TD
5	2D	LA-LB	TA-TB

^a HA and HB were placed at the five locations.

(d) Specimen 8 and 9

Figure B.3. Strain gauge locations.

Concrete Strains

Specimens were instrumented with a truss arrangement of Linear Variable Differential Transformers (LVDTs). This arrangement allows the uncoupling of deformations into flexural, shear, axial, and dilative components. Figure B.4 shows the LVDT truss arrangement, while Table B.5.2 specifies the placement and distances for the truss bays for each specimen.

Each LVDT was carefully attached at both ends to rods that were placed and cast inside the column core. The instrument measures the relative displacement between each anchor rod, which, when divided by the distance between rods, provides the average strain over that length. By obtaining the strain at the top and bottom chords, it is possible to calculate the average discrete section curvature. Since this is an average curvature over a length and not a continuous measurement, the curvature should be considered a lower boundary of the actual curvature.

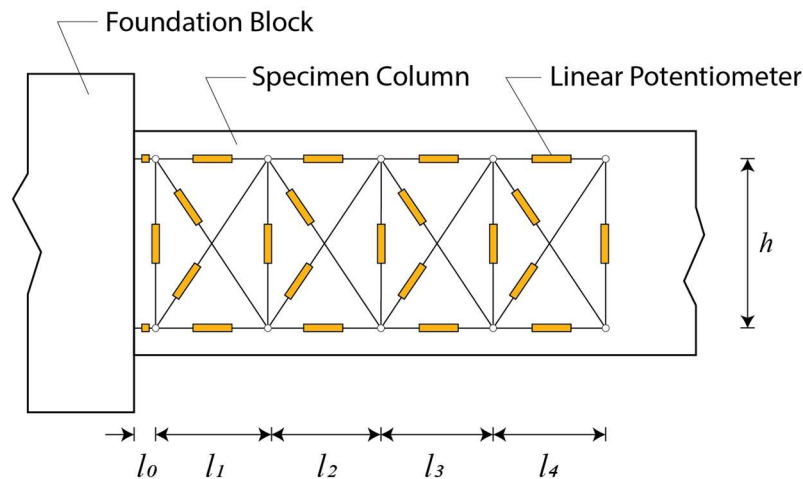


Figure B.4. Linear potentiometer gauge lengths.

Table B.5.2. Linear potentiometer gauge lengths.

Dimension (in)	Specimen 1 and 2	Specimen 3 to 7	Specimen 8 and 9
h	24	18	16
l_0	2	3	3
l_1	16	12	10
l_2	16	12	11
l_3	17	13	12
l_4	17	16	13.25

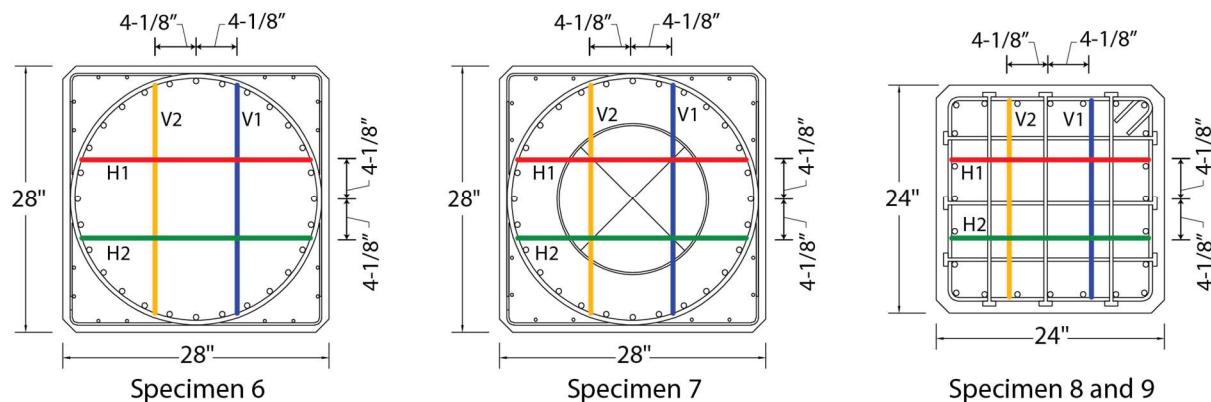
After the fifth test specimen, the limitations of using LVDTs to measure curvatures became evident. The instruments were easily damaged by spalling debris during testing, could only instrument a short region of the column length (2D), and could not measure the maximum curvature or peaks. Therefore, for the last four specimens, fiber optics were introduced to measure a continuous strain profile over the entire column length.

Four loops of fiber optics were placed in each specimen before casting, entering and exiting through the foundation block. Each loop was assigned a name: V1 and V2 for the vertical loops, and H1 and H2 for the horizontal loops. Figure B.5a illustrates the location of the cables for Specimens 6 to 9 in plan and elevation views, while Figure B.5b shows the location of the fiber optics in the specimens' cross sections.

The fiber optics presented several advantages over the LVDTs. They were not damaged by falling debris in the early stages and provided a continuous strain profile along the entire column length. This continuous profile allows for the identification of the true maximum curvature and peaks. Additionally, placing the fiber optics at different distances from the section's neutral axis enables analysis of the strain profile at a section, verifying the assumption that plane sections remain plane during the test. The major advantage over LVDTs is the ability to obtain continuous strain profiles along the column length.



(a) Fiber Optic cables location in plan and elevation.



(b) Fiber Optic cables location in cross sections.

Figure B.5. Fiber optic replacement.

B.2. Reinforcement steel properties

Steel reinforcement used in the experimental program was specified to meet ASTM A706 Grade 60 specifications except for the No. 2 wires. Table B.5.3 present the reinforcing steel properties of the steel reinforcement used in each test specimen. The data was obtained through laboratory testing of coupon tests.

Table B.5.3. Reinforcing steel properties.

Specimen	Type		E (x10 ⁴ ksi)	Fy (ksi)	ϵ_y	Fu (ksi)	ϵ_u
1-2	Longitudinal	No. 5	2.74	64.7	0.003	96.0	0.12
		No. 4	2.87	66.8	0.003	96.8	0.11
	Transverse	No. 3	3.07	75.3	0.004	99.5	0.08
3	Longitudinal	No. 5	2.74	64.7	0.003	96.0	0.12
		No. 3	2.79	67.7	0.003	106.8	0.08
	Transverse	No. 4	3.14	61.4	0.003	93.3	0.11
		No. 3	3.21	75.6	0.003	100.7	0.09
4	Longitudinal	No. 5	2.74	64.7	0.003	96.0	0.12
		No. 3	2.79	67.7	0.003	106.8	0.08
	Transverse	No. 4	3.14	61.4	0.003	93.3	0.11
		No. 2	3.22	51.5	0.003	54.1	0.13
5	Longitudinal	No. 5	2.74	64.7	0.003	96.0	0.12
		No. 3	2.79	67.7	0.003	106.8	0.08
	Transverse	No. 4	3.14	61.4	0.003	93.3	0.11
		No. 2	3.22	51.5	0.003	54.1	0.13
6	Longitudinal	No. 5	2.61	67.9	0.003	94.2	0.18
		No. 3	2.92	60.4	0.002	87.5	0.05
	Transverse	No. 3	2.98	78.6	0.004	96.4	0.06
		No. 2	2.86	39.2	0.001	50.3	0.19
7	Longitudinal	No. 5	2.46	60.4	0.003	90.7	0.15
		No. 3	2.92	60.4	0.002	87.5	0.05
	Transverse	No. 3	2.98	78.6	0.004	96.4	0.06
		No. 3	2.86	39.2	0.001	50.3	0.19
	Pipe	-	3.03	53.5	0.004	62.4	0.07
8	Longitudinal	No. 5	2.92	64.7	0.002	92.6	0.11
	Transverse	No. 3	2.87	67.9	0.003	104.1	0.07
		No. 3	2.53	65.7	0.004	101.5	0.11
9	Longitudinal	No. 5	2.92	64.7	0.002	92.6	0.11
	Transverse	No. 3	2.87	67.9	0.003	104.1	0.07
		No. 3	2.53	65.7	0.004	101.5	0.11